J. Earth Syst. Sci. (2021)130 190
https://doi.org/10.1007/s12040-021-01682-3

A sensitivity study of WRF model microphysics and cumulus parameterization schemes for the simulation of tropical cyclones using GPM radar data

Harish Baki, Sandeep Chinta, C Balaji* and Balaji Srinivasan

Indian Institute of Technology Madras, Chennai, India.
**Corresponding author. e-mail: balaji@iitm.ac.in*

MS received 20 November 2020; revised 19 March 2021; accepted 26 April 2021

The present study focuses on determining the best combination of microphysics (MP) and cumulus parameterization (CP) schemes for the simulation of Tropical Cyclones (TCs) in the Indian subcontinent region, using the Weather Research and Forecasting (WRF) model. From the available schemes, four CP schemes, namely Kain–Fritsch, Betts–Miller–Janjic, New Simplified Arakawa–Schubert, and Grell–Devenyi, and four MP schemes, namely WSM6, Purdue Lin, Thompson, and Morrison, are selected for the sensitivity study. Seven TCs are simulated using all combinations of the chosen physics schemes. The simulated tracks and intensities are compared against the India Meteorological Department (IMD) observations. The results show that the Kain–Fritsch scheme, in combination with all MP schemes, predicts the tracks best among all the available CP schemes, but the performance of microphysics schemes is indistinguishable. A further study is conducted using the Global Precipitation Measurement (GPM) radar data to identify the best MP scheme by comparing the reflectivities. An existing radar simulator is modified to calculate the simulated reflectivities from the WRF model output corresponding to the MP schemes. The simulated reflectivities are compared against the GPM radar reflectivities, and the results show that the Thompson scheme reproduces the reflectivities closest to observations. The performance of the best set of schemes obtained from this study is compared with a random set of schemes for cyclone Bulbul, and the best set of schemes outperformed the random schemes in every aspect.

Keywords. Weather Research and Forecasting (WRF) model; microphysics schemes; cumulus physics schemes; GPM radar data; forward radar operator; cloud resolving model; radar simulator (CR-SIM).

1. Introduction

The Indian subcontinent is prone to tropical cyclones (TCs) that form in the Indian Ocean during both the pre-monsoon (April–May) and post-monsoon (October–November) seasons. These tropical cyclones bring heavy rainfall and cause widespread destruction of life and property. A monsoon trough is a climatologically preferred zone for cyclone formation, which positions over 20°N at the beginning of the monsoon and moves over 5°N at the end of the season. During the monsoon season, the depressions still form over the warm waters near the coast, but they fail to intensify due to the vertical wind shear which removes the available heating by means of convection. Thus, the frequency of tropical cyclones in the monsoon season is quite less compared to the

Published online: 14 September 2021

pre-monsoon and post-monsoon seasons (Alam *et al.* 2003). Studies of track data of cyclones during the past 30 years reveal that the changes in the environmental parameters may lead to an increase in the intensity of post-monsoon tropical cyclones over the Bay of Bengal (BoB) region in the future (Balaguru *et al.* 2014). An extensive study of past 100 years of cyclone track data indicates the present global warming conditions increase the intensification of tropical cyclones over the BoB region (Rao *et al.* 2019). Furthermore, studies of Reddy *et al.* (2021) showed that future projections of present global warming conditions and climate change might lead to an intensification of tropical cyclones in their severity during the landfall. Consequently, accurate prediction of the cyclone track and its intensity during the landfall is very critical for the prevention of huge loss of lives and property.

Operational forecasting of the tropical cyclones is achieved through Numerical Weather Prediction (NWP) models. The NWP models can be categorized into global models, which operate at a resolution of tens to hundreds of kilometers, and regional mesoscale models, which operate at a much fine resolution. The regional models use the initial and lateral boundary conditions from the global models and simulate the weather phenomena. With the advancement in computational resources, the accuracy in the prediction of tropical cyclones using mesoscale models has increased to a large extent (Elsberry 2014; Yamaguchi *et al.* 2017). Nevertheless, the accuracy of an operational mesoscale model depends on various aspects, namely initial and boundary conditions, domain resolution, and specification of physics parameterization schemes. Researchers have been using regional mesoscale models such as Weather Research and Forecasting model (WRF) (Mukhopadhyay *et al.* 2011), Fifth-Generation Penn State/NCAR Mesoscale Model (MM5) (Rogers *et al.* 2007), and the Tropical Cyclone Model (TCM3) (Franklin *et al.* 2005) to name a few, for the prediction of tropical cyclones. Due to the availability and applicability for research and operational weather prediction over a broad spectrum of scales ranging from meters to thousands of kilometers, the WRF model is considered as a better model for numerical experiments in the current study.

The WRF model is a community-based numerical weather prediction and atmospheric simulation system, which has been extensively used in simulations of TCs over the North Indian Ocean (NIO) by many researchers (Pattanaik and Rao 2009; Mukhopadhyay *et al.* 2011; Chandrasekar and Balaji 2012; Osuri *et al.* 2012; Pattanayak *et al.* 2012; Srinivas *et al.* 2013; Taraphdar *et al.* 2014; Kanase and Salvekar 2015; Choudhury and Das 2017; Sandeep *et al.* 2018) and presented their insights to achieve a better forecast. Pattanaik and Rao (2009) indicated that the WRF model forecast errors of cyclone track and landfall time are reduced when the simulation is initialized 72 hrs before the landfall and concluded that the model simulations are dependent on initial conditions and domain resolutions. Mukhopadhyay *et al.* (2011) studied the importance of moist processes on the track and intensity prediction of tropical cyclones over NIO and reported that the Kain–Fritsch (KF) cumulus scheme in combination with WRF Single Moment 6-class (WSM6) microphysics scheme at 10 km grid scale reproduced the cyclone track and intensity close to observations. The authors explained the importance of graupel production in the intensification of the cyclone and its correlation with the vertical heating profile by means of latent heating at the middle level of the storm. Pattanayak *et al.* (2012) studied the impact of parameterization schemes on cyclone Nargis's track and intensity and reported that the movement of the cyclone is more sensitive to the cumulus scheme. Osuri *et al.* (2012) conducted a sensitivity study of CP and PBL schemes for five tropical cyclones and reported that Kain–Fritsch (KF) for CP and Yonsei University Scheme (YSU) for PBL schemes have better predictions for the track, intensity, and rainfall consistently. Srinivas *et al.* (2013) have conducted 65 sensitivity simulations for 21 cyclones on a double nested domain with 9 km fine resolution and reported that KF for CP, YSU for PBL, and Purdue Lin (Lin) for MP is the best combination for cyclone track and intensity prediction. Taraphdar *et al.* (2014) studied the influence of moist processes on the error growth and intrinsic predictability of tropical cyclones over NIO by performing numerical experiments with KF and WSM6 moist schemes and reported that the buoyancy associated with moist convection predominantly controls the error growth. The authors also examined the influence of domain resolution on error growth and observed that 10 km and 1.1 km resolutions followed closely in terms of error doubling time. Kanase and Salvekar (2015) conducted a sensitivity study of CP, MP, and PBL schemes for the simulations of two severe cyclonic storms on a triply nested domain with 6.6

km fine resolution. The authors reported that the cyclone track is more sensitive to the cumulus scheme, whereas intensity is more sensitive to MP and PBL schemes. Choudhury and Das (2017) conducted the sensitivity study of microphysics schemes for the simulations of three very severe cyclones on a double nested domain with 3 km fine resolution and reported that Thompson and Goddard scheme provides the highest skills in intensity. Sandeep *et al.* (2018) studied the sensitivity of cumulus and microphysics schemes for the simulations of tropical cyclone Vardah and reported that New Simplified Arakawa–Schubert (NSAS) for CP and Kessler Scheme (KS) for MP is the best combination for track and intensity prediction.

Researchers have been using reflectivity fields to investigate the differences among the physics schemes by comparing the simulated and observed reflectivity fields. Rogers *et al.* (2007), Zhu and Zhang (2006) examined the accuracy of model simulations compared with the observations for hurricanes (Bonnie 1998 and Floyd 1999), and reported that the simulations overestimate the reflectivities below the melting layer and above which the decrements in the reflectivities with height are very less. Min *et al.* (2015) evaluated the accuracy of microphysics schemes in simulating the summer monsoon and convective precipitation cases over the Korean Peninsula during 2011 using the radar reflectivity fields. Starzec *et al.* (2018) investigated the accuracy of two microphysics schemes in simulating the convective structure and convective depths over several months of regional forecasts using the reflectivity fields, and found that the near surface fields are well simulated but differ in vertical direction both from observations and from each other. Huang *et al.* (2020) performed a comparison of three microphysics schemes for the simulation of an extreme rainfall event in the coastal metropolitan city of Guangzhou, China. The authors reported that the simulated reflectivity fields in terms of intensity and coverage are similar for different microphysics schemes, whereas their vertical structures differ considerably. These studies suggest that the reflectivity fields can be used for the evaluation of microphysics schemes for the simulations of tropical cyclones over the Indian Ocean region.

The best combination of parameterization schemes that are performing well in the Indian Ocean region was proposed by various studies based on the track and intensity predictions. In contrast, their capability to reproduce reflectivities has not been established thus far. So, there exists a need to identify the best set of parameterization schemes that can accurately predict the tropical cyclone track, intensity, and reflectivities for the simulation of tropical cyclones. This will also help in better predictions of such extreme events in a future warming environment. This study investigates the sensitivity of four cumulus and four microphysics schemes for the simulations of seven tropical cyclones to ascertain their capability of reproducing reflectivities close to the GPM reflectivities on a triply nested domain with a fine resolution of 2 km, using the WRF model. The sensitivity experiments of cumulus schemes are performed based on the cyclone track, and intensity prediction similar to approaches reported earlier (Mukhopadhyay *et al.* 2011). The sensitivity experiments of microphysics schemes study their capability of reproducing the reflectivities in comparison with the GPM reflectivities and ascertain the reasons behind the deviations with respect to the observations.

Section 2 contains the details of the data used and a detailed methodology of the sensitivity study. Results of the model simulations compared with the observational data are discussed in section 3. Section 4 contains the conclusions obtained from this study.

2. Model description, events simulated, data, and methodology

2.1 *Model description*

In the present study, the Advanced Research WRF (WRF-ARW) model version 3.9.1 (Skamarock *et al.* 2008) is used to simulate the tropical cyclones. The WRF model is a community-based numerical weather prediction (NWP) and atmospheric simulation system. The dynamic core of the model solves the compressible, non-hydrostatic flux form of the Euler equations. The physical processes which cannot be resolved to the model grid are represented empirically/statistically using parameterization. The details of model description are presented in table 1. The selected tropical cyclones in the present study are originated from the Northern Indian Ocean. As the domain d03 does not cover the entire cyclone-affected zone, the center of the domain is changed according to the cyclone-affected zone for each cyclone. This way, the entire domain shifts at the cyclone-affected

Table 1. *Overview of the WRF model configuration.*

Model configuration	Details
Initial and lateral boundary conditions data	FNL 0.25° × 0.25° data
Input data interval	6 hrs
Model integration time	84 hrs
Horizontal resolution	18 km (D1) 6 km (D2) 2 km (D3)
Number of horizontal grid points	500 × 500 (D1) 901 × 901 (D2) 1501 × 1501 (D3)
Number of vertical layers	49
Integration time step	60 s, 20 s, 6.66 s

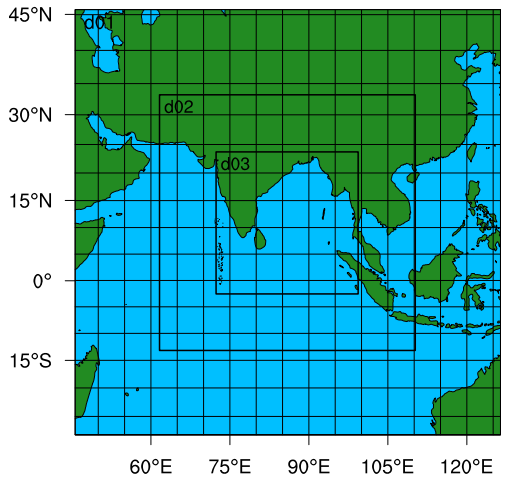

Figure 1. Configuration of the WRF model domains used for the simulations of cyclone Vardah.

zone. For reference, the domains used for one cyclone are illustrated in figure 1. The cyclones are simulated for 84 hrs, including the 12 hrs of spin-off time. A total of four CP schemes, namely Kain–Fritsch (KF) scheme (Kain 2004), Betts–Miller–Janjic (BMJ) scheme (Janjić 1994), New Simplified Arakawa–Schubert (NSAS) scheme (Han and Pan 2011), and Grell–Devenyi Ensemble (GD) scheme (Grell and Dévényi 2002), and total of four MP schemes, namely WRF Single-Moment 6-class scheme (WSM6) (Hong *et al.* 2004), Purdue Lin scheme (Lin) (Chen and Sun 2002), Thompson scheme (Thompson *et al.* 2008), and Morrison scheme (Morrison) (Morrison *et al.* 2009) are selected for the sensitivity experiments. The remaining parameterization schemes used in this study are: Yonsei University Scheme (YSU) (Hong *et al.* 2006) for planetary boundary layer physics, rapid radiative transfer model for global circulation models (RRTMG) scheme (Iacono *et al.* 2008) for shortwave radiation, rapid radiative transfer model (Mlawer *et al.* 1997) for longwave radiation, Unified Noah Land Surface Model (Tewari *et al.* 2004) for land surface physics, and MM5 similarity scheme (Beljaars 2004) for surface layer physics.

2.2 *Cyclones selected for numerical simulations*

In the present study, a total of seven tropical cyclones that originated in the Bay of Bengal during the period of 2015 to 2019 are selected for the sensitivity experiments. They are cyclonic storm Maarutha (IMD 2017a) two severe cyclonic storms, namely Mora (IMD 2017b) and Phethai (IMD 2018a), two very severe cyclonic storms, namely Vardha (IMD 2016) and Titli (IMD 2018b), and two extremely severe cyclonic storms, namely Chapala (IMD 2015) and Fani (IMD 2019a). The cyclones are chosen from a variety of categories to generalize the experiments in order to ensure the robustness of the outcomes. Table 2 presents the details of the category and landfall time of the cyclones selected in the present study. The IMD observed tracks of the selected cyclones are illustrated in figure 2.

2.3 *Data*

The observed data for the selected cyclones under consideration are available through the India Meteorological Department (IMD) (IMD 2015, 2016, 2017a, b, 2018a, b, 2019a, b). Observation variables, such as Central Sea Level Pressure (CSLP), cyclone tracks, and Maximum sustained Surface Wind (MSW), are provided at three-hourly intervals. In the present study, these observations are used to verify the accuracy of simulations. In addition to this, reflectivity data observed by the Global Precipitation Measurement (GPM) is also used for the verification of simulation accuracy. The GPM mission was launched in 2014 as a direct replacement for the successfully completed Tropical Rainfall Measurement Mission (TRMM). The GPM core observatory carries an on-board Dual-frequency Precipitation Radar (DPR), which consist of the Ku band and Ka-band Precipitation Radars, namely KuPR and KaPR (Hou *et al.* 2014). The specifications of the GPM-DPR are listed in table 3. Since the KuPR has a broad swath, the L2 product of KuPR, specifically *zFactorCorrected*, is used for the model verification. The GPM satellite orbits the earth 16 times a

Table 2. *Overview of the tropical cyclones selected in this study and corresponding GPM overpasses.*

Cyclone	Landfall time	Simulation duration	GPM overpass time	Orbit no.
CS Maarutha	0100–0200 UTC of 30th Dec 2011	2017-04-13_12:00:00 to 2017-04-17_00:00:00	2017-04-15 13:47:00	017781
SCS Mora	0400–0500 UTC of 30th may 2017	2017-05-26_18:00:00 to 2017-05-30_06:00:00	2017-05-29 00:50:00	018457
SCS Phethai	1400–1500 UTC of 17th Dec 2018	2018-12-14_06:00:00 to 2018-12-17_18:00:00	2018-12-14 15:17:00	027239
VSCS Vardah	0930–1030 UTC of 12th Dec 2016	2016-12-09_00:00:00 to 2016-12-12_12:00:00	2016-12-12 02:44:00	015845
VSCS Titli	2300 UTC of 10th–0000 UTC of 11th Oct 2018	2018-10-07_12:00:00 to 2018-10-11_00:00:00	2018-10-09 23:18:00	023218
ESCS Chapala	0100–0200 UTC of 3rd Nov 2015	2015-10-30_18:00:00 to 2018-11-03_06:00:00	2015-10-31 03:21:00	009498
ESCS Fani	0230–0430 UTC of 3rd May 2019	2019-04-29_18:00:00 to 2019-05-03_06:00:00	2019-05-01 12:01:00	029384

day and covers from −66.28° south to 66.28° north. It is observed that all cyclones have multiple GPM overpasses, but only a few overpasses have captured the cyclone's structure well. Thus, for each cyclone, only one strongest overpass is considered in this study. The details of the GPM overpasses over the selected tropical cyclones are listed in table 2.

2.4 *Methodology*

Using the combinations of selected CP and MP schemes which are listed in table 4, a total of seven tropical cyclones are simulated. This lead to a total of 112 numerical simulations. Each cyclone is simulated for 84 hrs, which includes 12 hrs of spin-off time and 72 hrs of simulation before landfall. The simulation initialization time and the duration are listed in table 2. Since the resolution of the domain d03 is 2 km, the cumulus parameterization is excluded in this domain to resolve the convection explicitly. Though the second domain d02 has a resolution of 6 km, which clearly indicates a grey zone, the cumulus scheme is implicitly taken in this domain based on the studies of Kanase and Salvekar (2015), Pennelly *et al.* (2014), Yano *et al.* (2015). The output variables, such as CSLP, cyclone track, and MSW, are chosen for the model verification. The root-mean-square (RMSE) errors of cyclone track, CSLP, and MSW are calculated against the IMD observations and are compared for each numerical experiment.

A further study is conducted to verify the performance of the considered microphysics schemes in simulating the reflectivities by comparing them with the GPM radar data. In this study, the experiments with four microphysics schemes in combination with only one CP scheme, which resulted in better track predictions are considered. Since the GPM-KuPR reflectivity data is an instantaneous dataset, the model simulations are also rerun such that the model output stores the data at that particular GPM overpass time. From the model output, the simulated reflectivities are calculated using a radar simulator corresponding to the 13.6 GHz GPM-KuPR frequency. In the present study, Cloud resolving model Radar SIMulator (CR-SIM), developed by Oue *et al.* (2019), is used to calculate the simulated reflectivities. A flow chart of the CR-SIM is illustrated in figure 3. The output file from the WRF model is given to the CR-SIM, which extracts the model prognostic variables at every grid point, such as pressure (P), temperature (T), dry air density (ρ), hydrometeor mixing ratios (Q), and hydrometeor number concentrations (NQ). Based on these prognostic variables, the simulator identifies the hydrometeor type and calculates the corresponding particle size distribution (PSD) (see Appendix). The simulator then calculates the single-scattering amplitudes of each hydrometeor, using the T-matrix method, provided by Mishchenko and Travis (1998). Following, the reflectivities of each hydrometeor are calculated using the Mie-scattering theory (Ryzhkov *et al.* 2011), corresponding to the GPM-KuPR frequency. Although, the CR-SIM software is developed for various MP schemes, including the

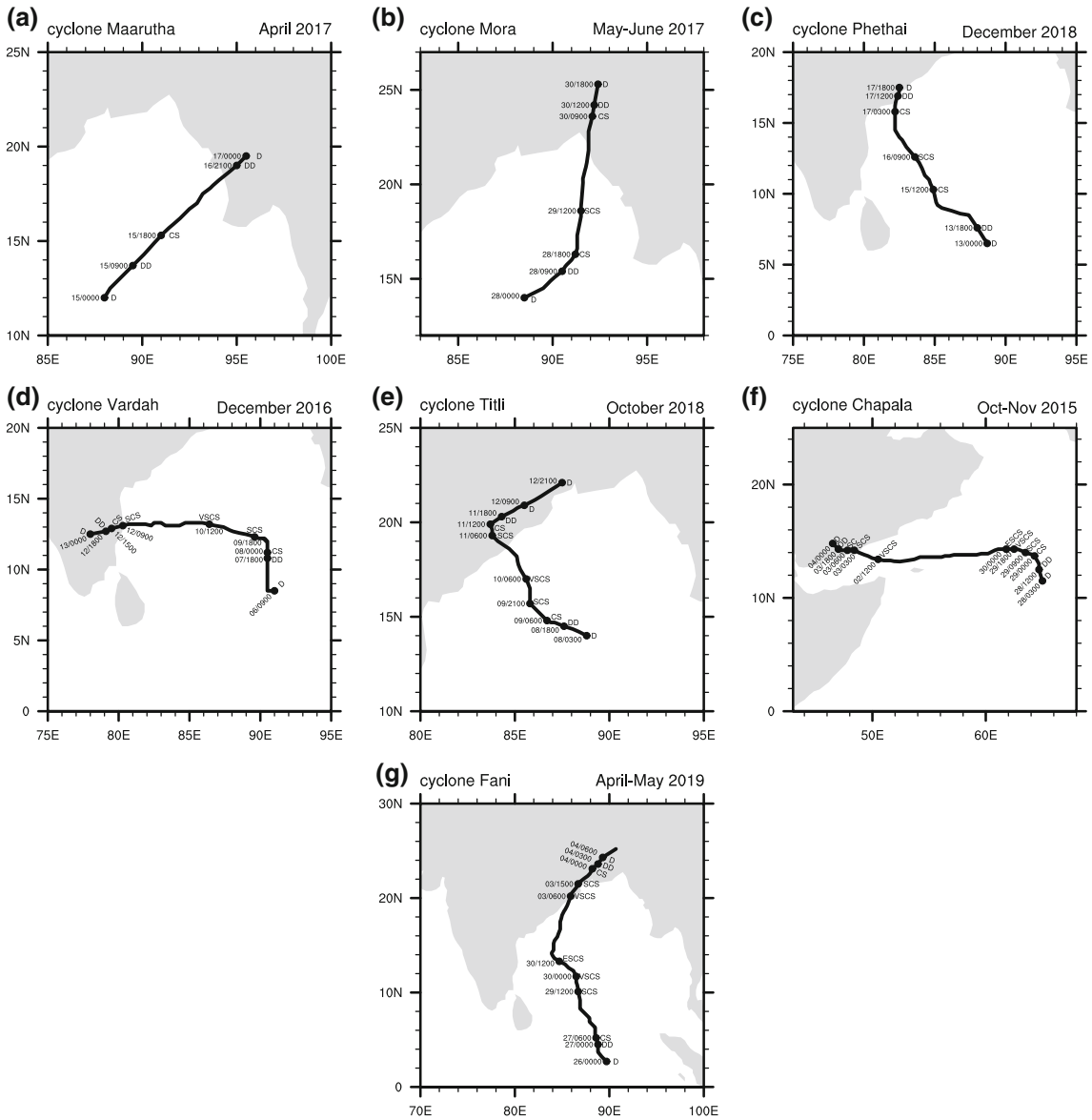

Figure 2. IMD observed tracks of the tropical cyclones, (**a**) Maarutha, (**b**) Mora, (**c**) Phethai, (**d**) Vardah, (**e**) Titli, (**f**) Chapala, and (**g**) Fani.

Thompson and Morrison schemes, some important schemes such as WSM6 and Lin are not included in the software. One of the major contributions from this study is the modification of the CR-SIM code to include these two MP schemes in the simulator.

Once the simulated reflectivities are calculated, they are validated against the GPM-KuPR reflectivities by using visual comparison and a fraction skill scores (FSS) comparison. Since the sensitivity of GPM-KuPR is <18 dBZ (Sun *et al.* 2020), reflectivities below 18 dBZ are discarded from the GPM-KuPR data, and the simulated reflectivity data. Studies of Kumar and Bhat (2016) reported that stratiform and deep convective clouds are the significant clouds in tropical storms, and the stratiform clouds dominate the storms. The cloud cell with reflectivity less than or equal to 40 dBZ at 3 km height and less than or equal to 30 dBZ at 8 km height is categorized as stratiform and convective otherwise. Based on these studies, two reference heights: 3 km and 8 km, and two thresholds: 40 dBZ at 3 km and 30 dBZ at 8 km, are selected for qualitative and quantitative analyses. The reflectivities at 3 km and 8 km are plotted on a 2D lat.–long. grid for a visual comparison. The FSS, as formulated by Roberts and Lean (2008), is a measure of verifying the accuracy of intensity. The FSS attains a value of 1 in a case where the intensity threshold is set to cover the entire intensity range. Since the stratiform clouds

have more occurrence, it is advisable to select thresholds of stratiform clouds, that is, ≤40 dBZ at 3 km height and ≤30 dBZ at 8 km height. The bias fields are calculated corresponding to each threshold for radar observations and model simulations using equations (1 and 2). Since the effect of forecast grid-scale is not studied here, a one-grid point is selected as a uniform length scale based on the study conducted by Roberts and Lean (2008), and the corresponding fractions are calculated for the observations and simulations using equations (3 and 4). Finally, the FSS is calculated using equations (5, 6, and 7) at two heights combined to produce a single FSS for one simulation. The FSS calculations are detailed below.

Table 3. *GPM-DPR specifications.*

Radar	KuPR	KaPR
Frequency	13.6 GHz	35 GHz
Swath	245 km	120 km
Horizontal foot print resolution	5 km	5 km
Vertical resolution	250 m	250 m/500 m
Scan type	Normal Scan (NS)	High sensitivity Scan (HS), Matched Scan (MS)
Beam number	49 in NS	24 in MS, 25 in HS
Beam width	0.71 degrees	0.71 degrees
Pulse Repetition Frequency	4100–4400 Hz	4100–4400 Hz
Pulse width	two 1.667 μs pulses	two 1.667 μs in MS, two 2.324 μs pulses in HS
Wavelength	2.3 cm	0.88 cm

$$I_{O_{(3\text{ km})}} = \begin{cases} 1 & \text{for} \quad O_{dBZ} \le 40 \\ 0 & \text{for} \quad O_{dBZ} > 40 \end{cases}$$
$$I_{M_{(3\text{ km})}} = \begin{cases} 1 & \text{for} \quad M_{dBZ} \le 40 \\ 0 & \text{for} \quad M_{dBZ} > 40 \end{cases} \quad (1)$$

$$I_{O_{(8\text{ km})}} = \begin{cases} 1 & \text{for} \quad O_{dBZ} \le 30 \\ 0 & \text{for} \quad O_{dBZ} > 30 \end{cases}$$
$$I_{M_{(8\text{ km})}} = \begin{cases} 1 & \text{for} \quad M_{dBZ} \le 30 \\ 0 & \text{for} \quad M_{dBZ} > 30 \end{cases} \quad (2)$$

$$O_{(3\text{ km},\,8\text{ km})}(i,j) = \frac{1}{n^2}\sum_{k=1}^{n}\sum_{l=1}^{n} I_{O_{(3\text{ km},8\text{ km})}} \times \left[i+k-1-\frac{n-1}{2}, j+l-1-\frac{n-1}{2}\right] \quad (3)$$

Table 4. *Details of the numerical experiments.*

Experiment name	Cumulus scheme (no CP in D03)	Microphysics scheme	Comments
KF_WSM6	KF	WSM6	KF convection with WSM6 explicit cloud microphysics in D01 and D02, and no cumulus convection in D03.
KF_Lin	KF	Lin	Same as KF_WSM6 but with Lin microphysics.
KF_Thompson	KF	Thompson	Same as KF_WSM6 but with Thompson microphysics.
KF_Morrisonn	KF	Morrison	Same as KF_WSM6 but with Morrison microphysics.
BMJ_WSM6	BMJ	WSM6	BMJ convection with WSM6 explicit cloud microphysics in D01 and D02, and no cumulus convection in D03.
BMJ_Lin	BMJ	Lin	Same as BMJ_WSM6 but with Lin microphysics.
BMJ_Thompson	BMJ	Thompson	Same as BMJ_WSM6 but with Thompson microphysics.
BMJ_Morrisonn	BMJ	Morrison	Same as BMJ_WSM6 but with Morrison microphysics.
NSAS_WSM6	NSAS	WSM6	NSAS convection with WSM6 explicit cloud microphysics in D01 and D02, and no cumulus convection in D03.
NSAS_Lin	NSAS	Lin	Same as NSAS_WSM6 but with Lin microphysics.
NSAS_Thompson	NSAS	Thompson	Same as NSAS_WSM6 but with Thompson microphysics.
NSAS_Morrisonn	NSAS	Morrison	Same as NSAS_WSM6 but with Morrison microphysics.
GD_WSM6	GD	WSM6	GD convection with WSM6 explicit cloud microphysics in D01 and D02, and no cumulus convection in D03.
GD_Lin	GD	Lin	Same as GD_WSM6 but with Lin microphysics.
GD_Thompson	GD	Thompson	Same as GD_WSM6 but with Thompson microphysics.
GD_Morrisonn	GD	Morrison	Same as GD_WSM6 but with Morrison microphysics.

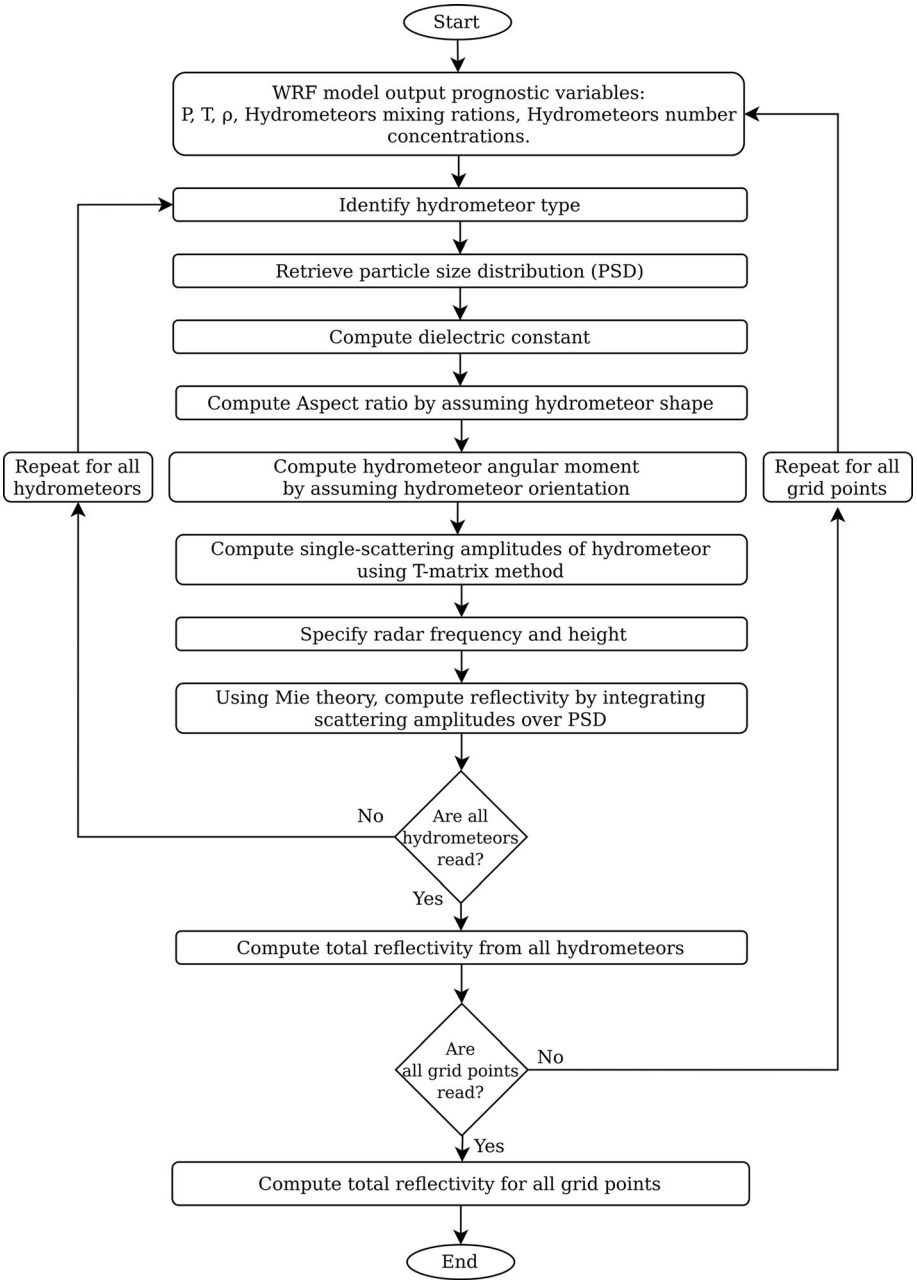

Figure 3. A flow chart of the CR-SIM forward radar operator.

$$M_{(3\text{ km},\,8\text{ km})}(i,j) = \frac{1}{n^2}\sum_{k=1}^{n}\sum_{l=1}^{n} I_{M_{(3\text{ km},8\text{ km})}} \times \left[i+k-1-\frac{n-1}{2}, j+l-1-\frac{n-1}{2}\right] \quad (4)$$

$$MSE = \frac{1}{Nx \times Nx}\sum_{i=1}^{Nx}\sum_{j=1}^{Ny} \Big[\big[O_{(3\text{ km})}(i,j) - M_{(3\text{ km})}(i,j)\big]^2 + \big[O_{(8\text{ km})}(i,j) - M_{(8\text{ km})}(i,j)\big]^2\Big] \quad (5)$$

$$MSE_{\text{ref}} = \frac{1}{Nx \times Ny}\sum_{i=1}^{Nx}\sum_{j=1}^{Ny}\Big[O^2_{(3\text{ km})}(i,j) + M^2_{(3\text{ km})}(i,j) + O^2_{(8\text{ km})}(i,j) + M^2_{(8\text{ km})}(i,j)\Big] \quad (6)$$

$$FSS = 1 - \frac{MSE}{MSE_{\text{ref}}}. \quad (7)$$

In the above equations, O stands for observations, M stands for model output, subscripts 3 km and 8 km stand for at 3 km and 8 km heights, respectively, I stands for the binary field, and n stands for

forecasting scale, that is equal to 1. The binary fields are calculated for every observation and model output, and for every threshold. The indices i, j are iterated for all grid points, and indices k, l are iterated for one grid point. Finally, the FSS is calculated for every threshold.

From the FSS comparison, the simulation with the highest FSS value is the best MP scheme. From this set of experiment, one can obtain the best combination of microphysics and cumulus physics schemes that has good accuracy in predicting the cyclone track and reflectivity. Once the best combination of physics schemes is obtained, the performance of these schemes is validated for other cyclones. For this purpose, cyclone Bulbul is simulated using a random set of schemes and the obtained best set. The random physics schemes consist of Grell–Freitas Ensemble Scheme (Grell *et al.* 2014) for cumulus and WDM5 scheme for microphysics (Lim and Hong 2010), while all the other schemes remain unchanged. The simulated cyclone track, intensity, and reflectivity are compared with the observations, and the performance of the best physics schemes is verified.

3. Results and discussion

In this section, the results of the numerical experiments related to the sensitivity study of cumulus parameterization (CP) schemes and microphysics (MP) schemes for the simulations of tropical cyclones are discussed in detail. The model simulated parameters such as cyclone track, SLP and MSW are first validated against the IMD observations to identify the best CP scheme. Once the best CP scheme is identified, the simulations with that CP scheme and 4 MP schemes are considered for GPM reflectivity validation. The simulated reflectivities are validated against the GPM-KuPR reflectivities.

3.1 *Sensitivity of the physics schemes to the cyclone track and intensity*

A comparison between the tracks and intensities of the cyclone simulations with respect to IMD observations is presented in this section. Figure 4 presents the simulated tracks of the selected cyclones for the numerical experiments listed in table 4, in comparison with IMD observations, at 3-hr interval. Each row of subfigures of 4 presents the simulated tracks that correspond to one cyclone. The numerical experiments of KF_WSM6, KF_Lin, KF_Thompson, and KF_Morrison are presented in all subfigures of the first column; BMJ_WSM6, BMJ_Lin, BMJ_Thompson, and BMJ_Morrison are presented in the second column; NSAS_WSM6, NSAS_Lin, NSAS_Thompson, and NSAS_Morrison are presented in the third column; and GD_WSM6, GD_Lin, GD_Thompson, and GD_Morrison are presented in the fourth column. Figure 4(a1–a4) presents the simulated tracks of cyclone Maarutha, which show that the variation of MP schemes has a negligible impact on the cyclone track for a particular CP scheme. The experiments with the KF scheme predicted the track well in agreement with the observations compared to the other CP schemes. Figure 4(b1–b4) presents the simulated tracks of cyclone Mora. Here too, the contribution of MP schemes towards the track prediction is minimal. The experiments of KF and BMJ CP schemes in combination with all MP schemes predicted the track accurately. Figure 4(c1–c4) presents the simulated tracks of cyclone Phethai, showing that all the MP schemes have followed the previous trend, and the KF scheme combined with all MP schemes accurately predicted the track. Figure 4(d1–d4) presents the simulated tracks of cyclone Vardah, which shows that all the MP schemes have followed a similar track for a particular CP scheme. The experiments of BMJ scheme in combination with all the MP schemes have predicted the track accurately. In contrast, the other CP schemes have deviated from observed track. Figure 4(e1–e4) presents the simulated tracks of cyclone Titli, which shows that the KF scheme, in combination with all MP schemes, had landfall, whereas the tracks of the remaining CP schemes ended up in the ocean. Even though the KF scheme with different MP schemes have deviated from the observed track, they have less track error during the landfall. Figure 4(f1–f4) presents the simulated tracks of cyclone Chapala, which show that all the simulations have similar track errors, with BMJ and GD CP schemes are seen to perform a little better compared to the other schemes. Figure 4(g1–g4) shows the simulated tracks of cyclone Fani. The KF scheme, in combination with all MP schemes, has followed the observed track. For the NSAS and GD schemes, the variation of MP schemes has negligible effect. However, for the KF and BMJ schemes, different MP schemes have variations in tracks. The composited daily (excluding the first 12 hrs of simulations) track errors of all cyclones for the stated numerical experiments are illustrated in

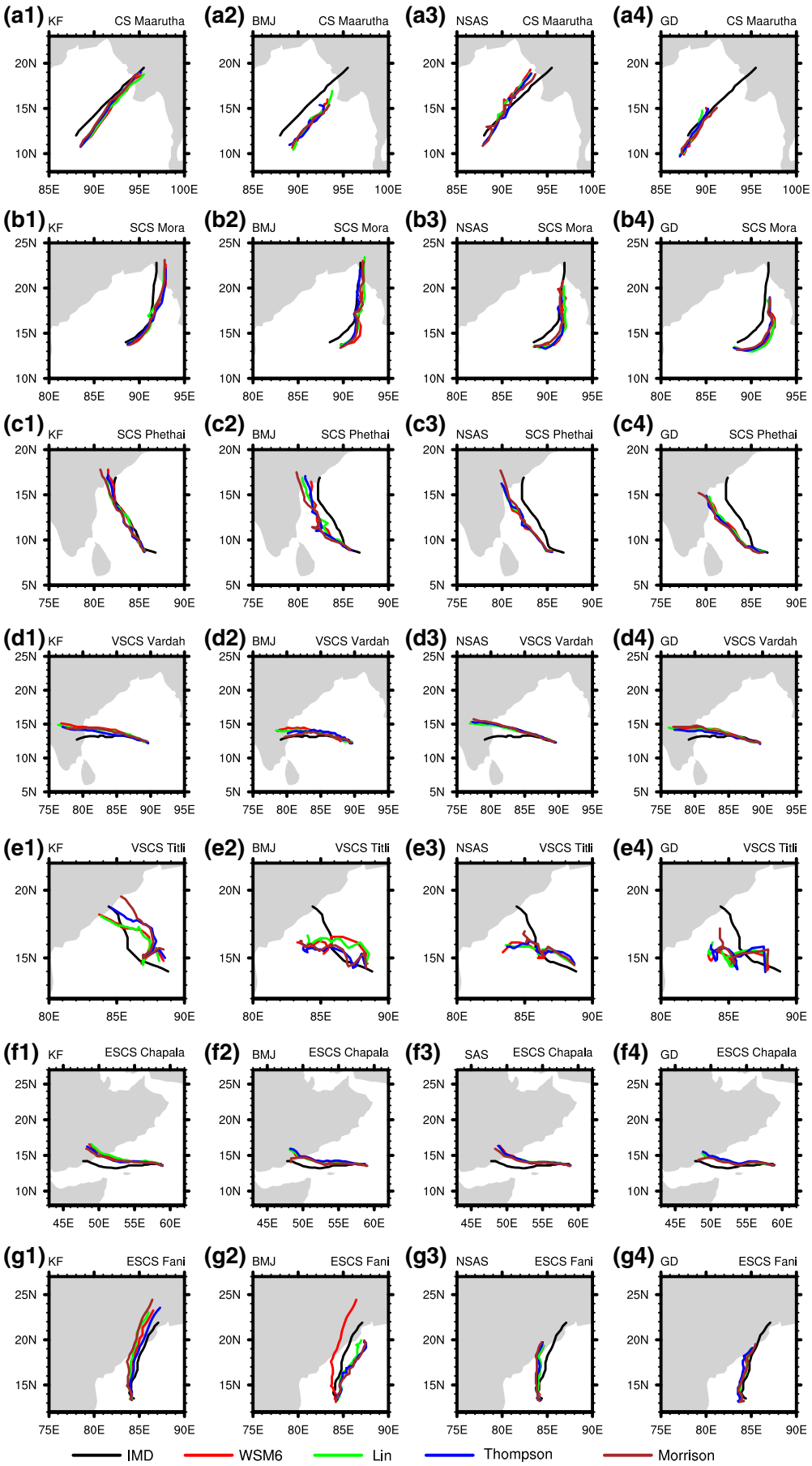
(a1) KF CS Maarutha
(a2) BMJ CS Maarutha
(a3) NSAS CS Maarutha
(a4) GD CS Maarutha
(b1) KF SCS Mora
(b2) BMJ SCS Mora
(b3) NSAS SCS Mora
(b4) GD SCS Mora
(c1) KF SCS Phethai
(c2) BMJ SCS Phethai
(c3) NSAS SCS Phethai
(c4) GD SCS Phethai
(d1) KF VSCS Vardah
(d2) BMJ VSCS Vardah
(d3) NSAS VSCS Vardah
(d4) GD VSCS Vardah
(e1) KF VSCS Titli
(e2) BMJ VSCS Titli
(e3) NSAS VSCS Titli
(e4) GD VSCS Titli
(f1) KF ESCS Chapala
(f2) BMJ ESCS Chapala
(f3) SAS ESCS Chapala
(f4) GD ESCS Chapala
(g1) KF ESCS Fani
(g2) BMJ ESCS Fani
(g3) NSAS ESCS Fani
(g4) GD ESCS Fani
IMD
WSM6
Lin
Thompson
Morrison

figure 8(a1–d1), which show that the variation of MP schemes has minimal impact on track prediction. The composited track errors of all the experiments at the end of the first day are 80 km, except the GD scheme, for which the track errors are around 110 km. The track errors of the KF experiments reached 120 km and 140 km at the end of the second and third days, respectively. In contrast, the track errors of the remaining schemes increased drastically and increased to more than 180 km at the end of the third day. From these results, it is evident that the cumulus scheme plays an important role in cyclone track prediction, and the KF scheme performed better than the remaining schemes.

Studies of Mukhopadhyay *et al.* (2011) suggest that the upper-level steering governs the movement of a cyclone. The velocity field of cyclone Fani at 200 hPa is illustrated in figure 5 to examine the effect of upper-level steering on cyclone track. Since the effect of MP schemes on track prediction is minimal, the experiments of each cumulus scheme combined with the WSM6 MP scheme are considered. An anticyclonic circulation governs the movement of cyclone Fani to the northeast of the system center, which can be clearly seen in figure 5. The velocity field of the KF_WSM6 experiment clearly shows a strong anticyclonic circulation besides a cyclonic circulation at the end of the first day. During the end of second and third days, the anticyclonic circulation moved northeast and reached Myanmar, whereas the cyclonic circulation closely followed it. The BMJ_WSM6 experiment produced a little weaker anticyclonic circulation at the end of first and second days, which lead to a deviation in the cyclone track. However, the NSAS and GD scheme did not simulate a well-defined anticyclonic circulation at the end of the first day, which lead to a time delay in the cyclone track. Similar results are obtained for other cyclones also (figures not shown). From the above results, it is evident that the KF scheme accurately simulates the upper level steering, which helps in better simulations of cyclone track.

A sensitivity study of the physics schemes to the cyclone intensity is carried by comparing the simulated Maximum Sustained Wind speed (MSW) and central Sea Level Pressure (SLP) with the IMD observations. The time evolution of the SLP and the MSW of the selected cyclones for the numerical experiments listed in table 4 are plotted in figures 6 and 7, respectively. Similar to figure 4, each row of subfigures in figures 6 and 7 corresponds to one cyclone and each column of subfigures corresponds to one CP scheme. The results indicate that the KF cumulus scheme experiments combined with all the MP schemes produced the highest intensity compared to the remaining experiments. The experiments of NSAS and GD schemes have relatively similar intensification, whereas the performance of the BMJ scheme is a little poor compared to the remaining schemes. The results also suggest that all the MP schemes follow similar time evolution for KF, NSAS, and GD schemes. For the BMJ scheme, the WSM6 closely followed the time evolution of observations and performed better than the remaining MP schemes. To quantitatively compare the results of different experiments, the normalized pattern statistics of SLP and MSW are computed and presented in Taylor diagrams (Taylor 2001). In the Taylor diagrams 8(a2–d2), distance from the origin to any point indicates the normalized standard deviation, distance from the reference point to any point indicates the root mean squared error (RMSE), and the cosine of position vector from the origin indicates the pattern correlation with the observations. The standard deviation of observations is indicated with a darker arc at the value 1. The experiments that are close to the reference point imply the best performance. The results suggest that all the experiments show a similar correlation at 0.9, and the performance of MP schemes is indistinguishable for the cyclone intensity prediction. From figure 8(c2), it is evident that experiments of NSAS with all MP schemes show relatively better performance, whereas the experiments of the KF scheme show the second-best performance.

Studies of Ma and Tan (2009) suggest that a possible reason for cyclone intensification is due to the potential vorticity field. To examine a better or worse performance in intensity prediction by the selected cumulus schemes, the potential vorticity field at the lower level (950 hPa) is illustrated in

Figure 4. The 84-hr simulated tracks of cyclones (**a1–a4**) Maarutha, (**b1–b4**) Mora, (**c1–c4**) Phethai, (**d1–d4**) Vardah, (**e1–e4**) Titli, (**f1–f4**) Chapala, and (**g1–g4**) Fani, using the experiments, compared with the IMD observed tracks, at 3-hr interval. (**a1–g1**) correspond to the experiments KF_WSM6, KF_Lin, KF_Thom, and KF_Morr. (**a2–g2**) correspond to the experiments BMJ_WSM6, BMJ_Lin, BMJ_Thom, and BMJ_Morr. (**a3–g3**) correspond to the experiments NSAS_WSM6, NSAS_Lin, NSAS_Thom, and NSAS_Morr. (**a4–g4**) correspond to the experiments GD_WSM6, GD_Lin, GD_Thom, and GD_Morr.

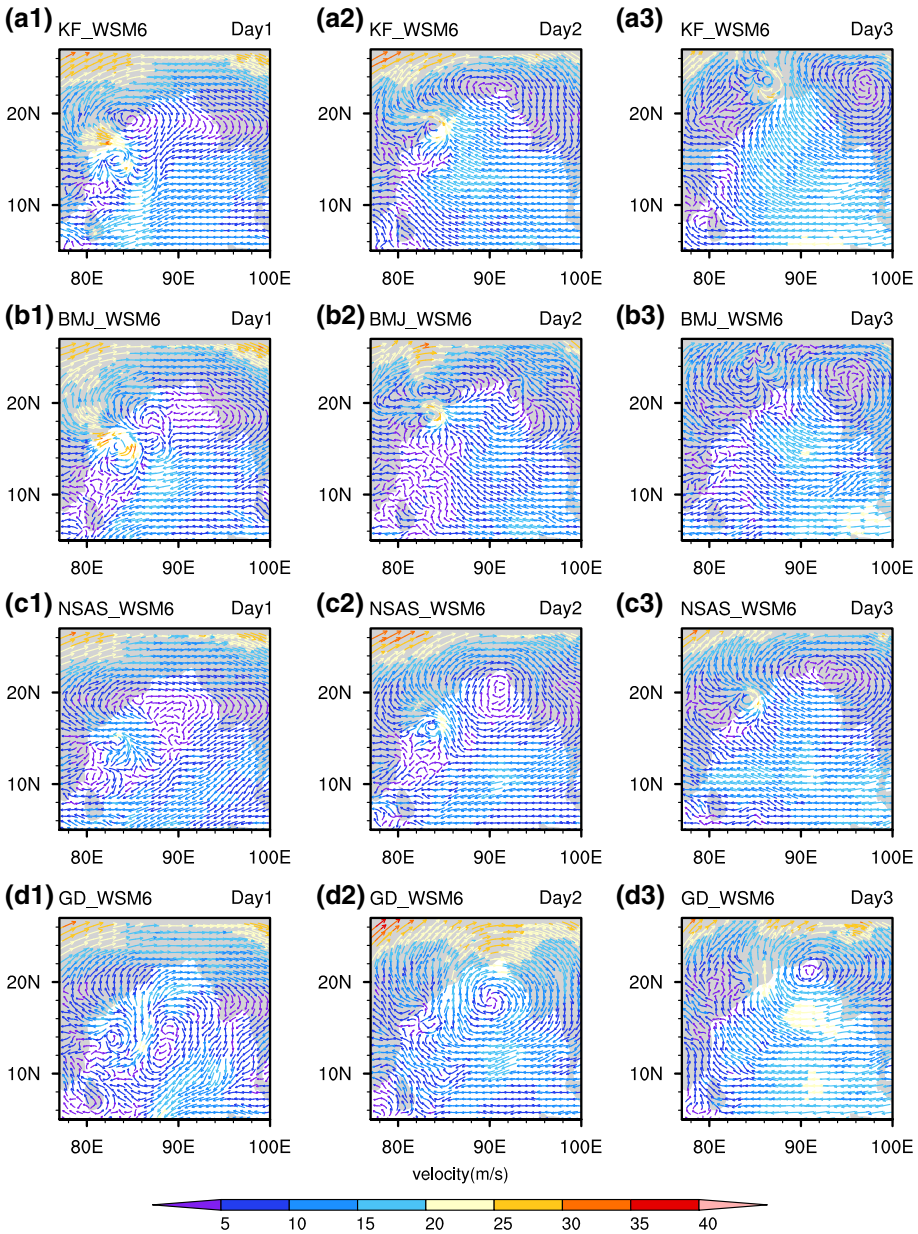

Figure 5. The upper level (200 hPa) velocity field of cyclone Fani simulated using (**a1–a3**) KF_WSM6, (**b1–b3**) BMJ_WSM6, (**c1–c3**) NSAS_WSM6, and (**d1–d3**) GD_WSM6 experiments. Figure (**a1–d1**) shows the velocity field at the end of first day, (**a2–d2**) second day, and (**a3–d3**) third day.

figure 9. The KF_WSM6 and BMJ_WSM6 experiments produced more localized small-scale potential vorticity disturbances during the entire simulation duration as shown in figure 9(a1–a3) and 9(b1–b3). The small-scale disturbance energy that was not consumed by the convection is available for the intensification of a cyclone (Ma and Tan 2009). In contrast, the NSAS_WSM6 and GD_WSM6 experiments produced very few small-scale localized disturbances, as shown in figure 9(c1–c3) and 9(d1–d3), which ultimately resulted in low intensification as seen in figures 6

Figure 6. The time evolution of central sea level pressure of cyclones (**a1–a4**) Maarutha, (**b1–b4**) Mora, (**c1–c4**) Phethai, (**d1–d4**) Vardah, (**e1–e4**) Titli, (**f1–f4**) Chapala, and (**g1–g4**) Fani, using the experiments, compared with the IMD observations, at 3-hr interval. (**a1–g1**) correspond to the experiments KF_WSM6, KF_Lin, KF_Thom, and KF_Morr. (**a2–g2**) correspond to the experiments BMJ_WSM6, BMJ_Lin, BMJ_Thom, and BMJ_Morr. (**a3–g3**) correspond to the experiments NSAS_WSM6, NSAS_Lin, NSAS_Thom, and NSAS_Morr. (**a4–g4**) correspond to the experiments GD_WSM6, GD_Lin, GD_Thom, and GD_Morr.

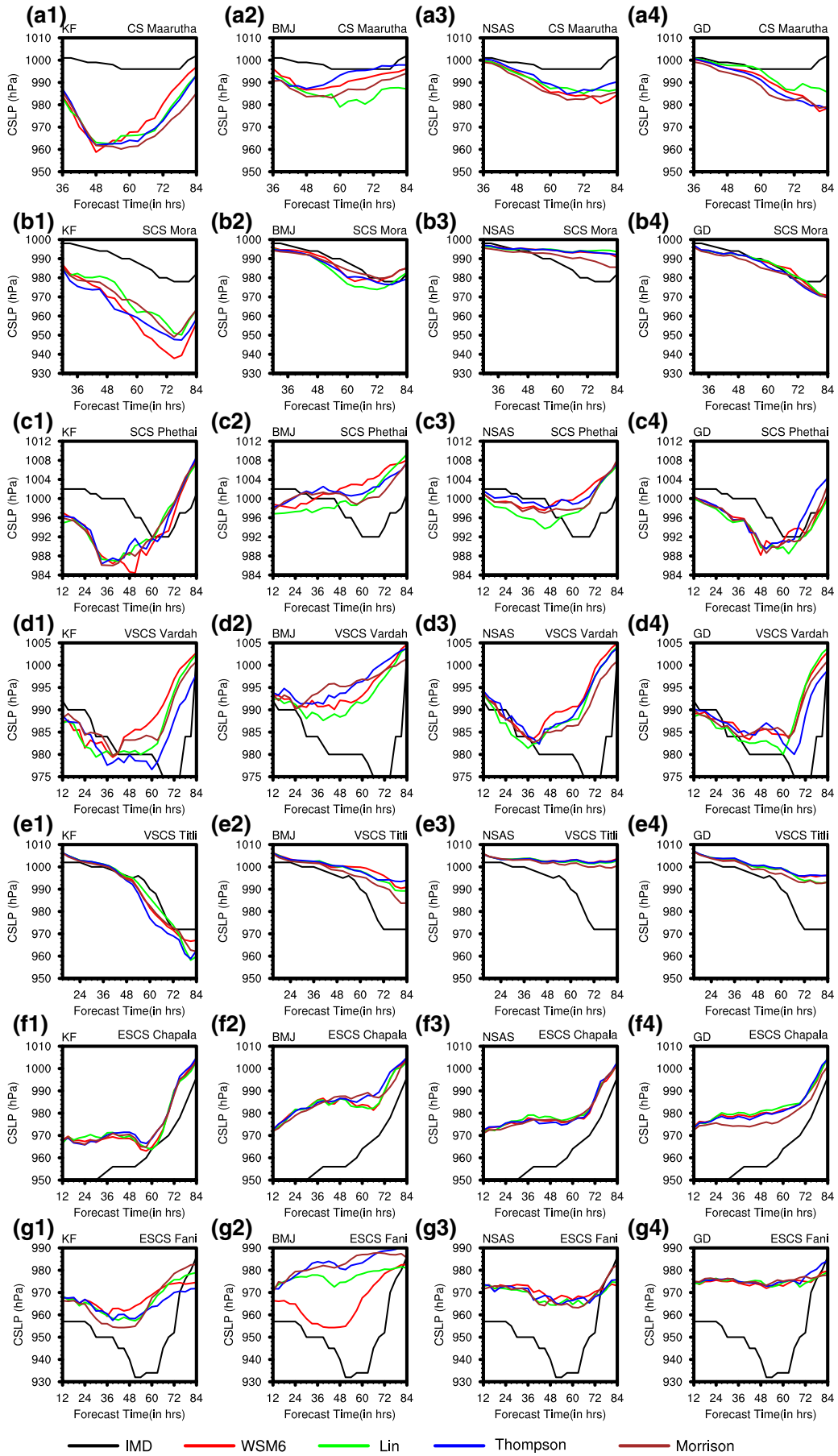
(a1) KF CS Maarutha
(a2) BMJ CS Maarutha
(a3) NSAS CS Maarutha
(a4) GD CS Maarutha
(b1) KF SCS Mora
(b2) BMJ SCS Mora
(b3) NSAS SCS Mora
(b4) GD SCS Mora
(c1) KF SCS Phethai
(c2) BMJ SCS Phethai
(c3) NSAS SCS Phethai
(c4) GD SCS Phethai
(d1) KF VSCS Vardah
(d2) BMJ VSCS Vardah
(d3) NSAS VSCS Vardah
(d4) GD VSCS Vardah
(e1) KF VSCS Titli
(e2) BMJ VSCS Titli
(e3) NSAS VSCS Titli
(e4) GD VSCS Titli
(f1) KF ESCS Chapala
(f2) BMJ ESCS Chapala
(f3) NSAS ESCS Chapala
(f4) GD ESCS Chapala
(g1) KF ESCS Fani
(g2) BMJ ESCS Fani
(g3) NSAS ESCS Fani
(g4) GD ESCS Fani
CSLP (hPa)
Forecast Time(in hrs)
IMD
WSM6
Lin
Thompson
Morrison

and 7. The sensitivity experiments related to the cyclone track and the intensity imply that the KF scheme, combined with all MP schemes, performed better than the remaining CP schemes.

3.2 *Sensitivity of microphysics schemes to the reflectivity*

In the sensitivity experiments related to the microphysics schemes, the simulations of the experiments, namely KF_WSM6, KF_Lin, KF_Thompson, and KF_Morrison, which resulted in better track and intensity prediction are considered. The simulated reflectivities from the model output are calculated using the CR-SIM forward radar operator for the GPM-KuPR frequency of 13.5 GHz and are validated against the GPM-KuPR reflectivity. Figures 10–12 present a visual comparison of the simulated reflectivities with respect to the GPM-KuPR reflectivity, for the selected cyclones, during their overpasses, which are specified in the table 2. In each figure, the first column of subfigures correspond to the GPM-KuPR reflectivity, and the subsequent columns correspond to the WRF simulations of KF_WSM6, KF_Lin, KF_Thompson, and KF_Morrison experiments, respectively. Similarly, the first row of the subfigures shows the reflectivity at 3 km altitude, and the second row shows the reflectivity at 8 km altitude. Apart from visual comparison, an FSS comparison is also performed to quantify the accuracy of the simulations. The parallel lines in each figure represent the path of GPM-KuPR and are drawn in every figure to show that the data in between these lines is only considered in quantitative analysis.

From figures 10–12, it is evident that most of the cloud cells observed by the GPM-KuPR are stratiform, i.e., having reflectivity less than 40 dBZ at 3 km altitude and less than 30 dBZ at 8 km altitude. The convective cells, which are characterized by reflectivity greater than 40 dBZ at 3 km and greater than 30 dBZ at 8 km altitude, are very few in number, and that too are observed at only the cyclone eyewalls. This is qualitatively demonstrated in figure 13, where the vertical cross-sections of simulated and observed reflectivities for cyclone Fani along the lateral and longitudinal lines which are passing through the cyclone wall are illustrated. Here, the longitudinal line is drawn parallel to the traveling path of the GPM radar, and the lateral line is drawn perpendicular to the traveling path, which are shown in figure 12(a1–a5). Figure 13(a1, a2) clearly shows that the deep convective clouds which rose beyond 8 km altitude with reflectivity greater than 30 dBZ are seen to dominate the cyclone eyewall. The stratiform clouds, which are characterized by the presence of a bright band, are seen everywhere other than the eyewall. The sensitivity experiments of the cyclone track revealed that the selected MP schemes have a very minimal impact on cyclone movement, which implies the simulated reflectivities correspond to each MP scheme will have a similar spatial structure. This can also be seen in figures 10–12, as the locations of the simulated reflectivities correspond to every overpass are identical for all the experiments. These results are in agreement with that of Huang *et al.* (2020). Though all the simulations have similarities in spatial structure, they failed to capture the cyclone eyewall even at the 2 km resolution, which can be clearly seen in figures 12 and 13. However, the main difference among the experiments arises in their vertical reflectivity structures. The reflectivities of the GPM-KuPR are sharply decreased beyond the bright band (at 5 km), which is only observed in the experiments of the Thompson scheme. The remaining experiments produced reflectivities with high intensities beyond the bright band. The reason for these differences can be attributed to the hydrometeor mixing ratios.

The hydrometeors govern the simulated reflectivity, which means that the amount, type, and drop size distribution collectively affect the calculation of simulated reflectivity. All the MP schemes have the same number of hydrometeors, but the essential difference arises from their drop size distributions (see Appendix A), which is a prime factor for the amount of hydrometeors that is estimated. The model simulated reflectivity is contributed by three hydrometeors: rain, snow, and graupel (Koch *et al.* 2005; Min *et al.* 2015).

Figure 7. The time evolution of maximum sustained wind speed of cyclones (**a1–a4**) Maarutha, (**b1–b4**) Mora, (**c1–c4**) Phethai, (**d1–d4**) Vardah, (**e1–e4**) Titli, (**f1–f4**) Chapala, and (**g1–g4**) Fani, using the experiments, compared with the IMD observations, at 3 hr interval. (**a1–g1**) correspond to the experiments KF_WSM6, KF_Lin, KF_Thom, and KF_Morr. (**a2–g2**) correspond to the experiments BMJ_WSM6, BMJ_Lin, BMJ_Thom, and BMJ_Morr. (**a3–g3**) correspond to the experiments NSAS_WSM6, NSAS_Lin, NSAS_Thom, and NSAS_Morr. (**a4–g4**) correspond to the experiments GD_WSM6, GD_Lin, GD_Thom, and GD_Morr.

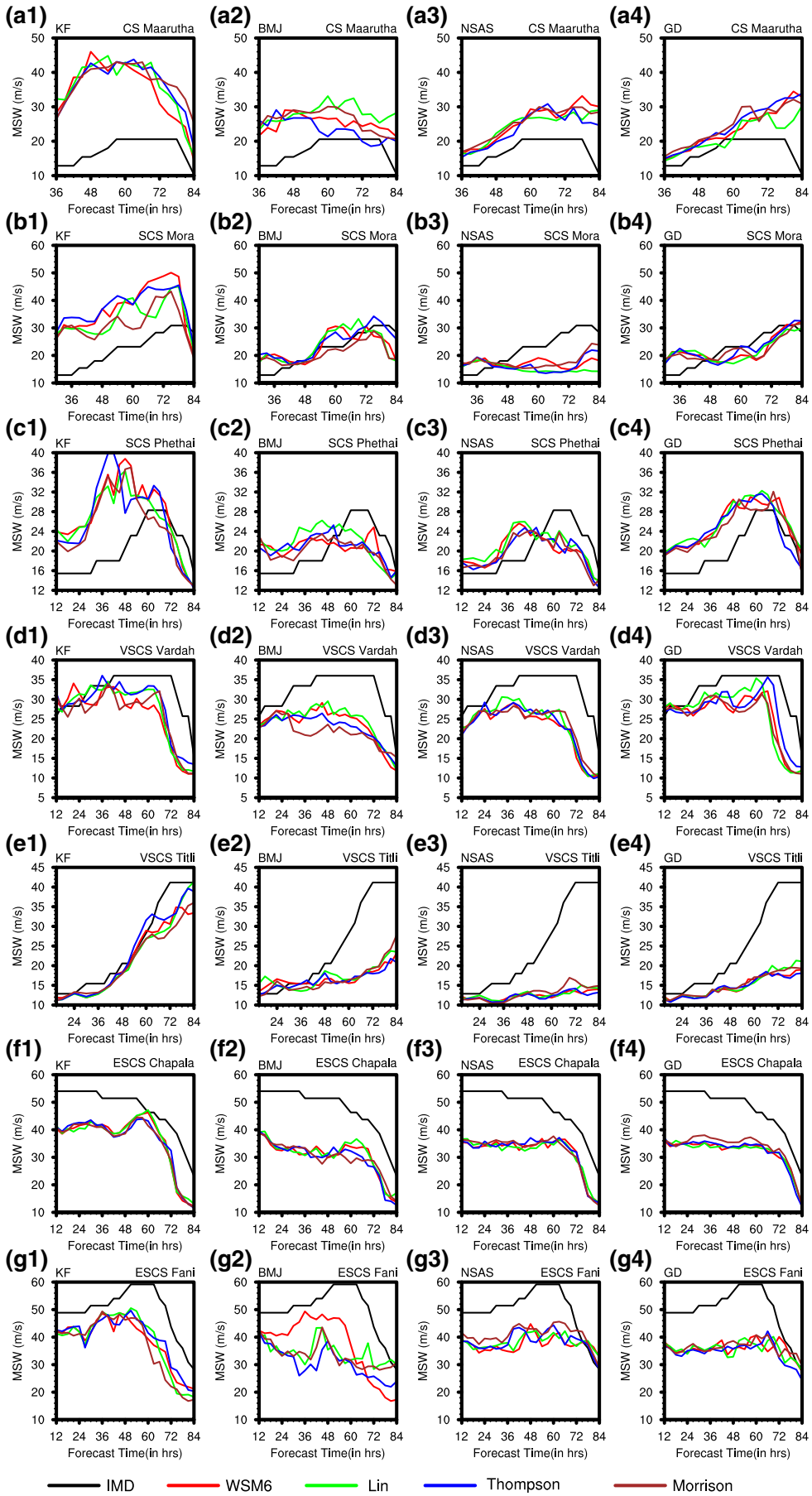
(a1) KF CS Maarutha
(a2) BMJ CS Maarutha
(a3) NSAS CS Maarutha
(a4) GD CS Maarutha
(b1) KF SCS Mora
(b2) BMJ SCS Mora
(b3) NSAS SCS Mora
(b4) GD SCS Mora
(c1) KF SCS Phethai
(c2) BMJ SCS Phethai
(c3) NSAS SCS Phethai
(c4) GD SCS Phethai
(d1) KF VSCS Vardah
(d2) BMJ VSCS Vardah
(d3) NSAS VSCS Vardah
(d4) GD VSCS Vardah
(e1) KF VSCS Titli
(e2) BMJ VSCS Titli
(e3) NSAS VSCS Titli
(e4) GD VSCS Titli
(f1) KF ESCS Chapala
(f2) BMJ ESCS Chapala
(f3) NSAS ESCS Chapala
(f4) GD ESCS Chapala
(g1) KF ESCS Fani
(g2) BMJ ESCS Fani
(g3) NSAS ESCS Fani
(g4) GD ESCS Fani
MSW (m/s)
Forecast Time(in hrs)
IMD
WSM6
Lin
Thompson
Morrison

Rain particles exist below the freezing level and above which the remaining two hydrometeors exist. This implies the reflectivities seen at 3 km altitude are solely contributed by rain particles, whereas the reflectivities seen at 8 km altitude are contributed by snow and graupel together. A clear look at the 3 km altitude reveals that all schemes have a very similar spatial structure with a few variations in their intensities. Since the WSM6 and Lin schemes have the same drop size distribution for rain, their simulated reflectivities at the 3 km level are also in the same order, which can be seen for all the cyclones. Though the Morrison scheme also has the same drop size distribution, its intercept and slope parameters are calculated based on the number concentration, which is a model simulated variable. In contrast, the Thompson scheme has different drop size distribution for rain with varying intercept parameters. These variations are clearly seen in the reflectivity intensities that are simulated by the respective MP schemes. Out of the four schemes, the Thompson scheme produces relatively similar intensities in comparison with GPM reflectivities for all cyclones. The Morrison scheme overestimated the intensities with the highest number of convective cells and also produced huge spatial coverage with stratiform clouds. The WSM6 and Lin schemes produce similar intensities and structure, but their intensities are higher than that of the Thompson scheme. The visual comparison at 8 km altitude shows that there exists much difference in the intensities and number of cloud cells of the reflectivities simulated by respective MP schemes. These variations can be attributed to the differences in drop size distributions of snow and graupel hydrometeors. The Thompson scheme, specially designed for snow and utilizes the hydrometeor mixing ratio for graupel intercept parameter, shows a close comparable intensity with that of GPM reflectivities. The Morrison scheme produces a large number of cloud cells at this level and overestimates the reflectivities. This can be attributed to the overestimation of the number concentrations of snow and graupel. The WSM6 and Lin schemes have the same graupel drop size distributions, but their size distribution for snow varies with intercept parameters. This variation in intercept parameter resulted in variations in the reflectivities, with WSM6 producing higher intensity compared to the Lin scheme. The reflectivity intensities of these two schemes are in between the Thompson scheme and the Morrison scheme. The order of magnitude of the simulated intensities corresponding to each MP scheme is relatively similar. Thus, a quantitative verification method is much needed to distinguish the performance of the physics schemes. Thus, the FSS is considered as a suitable verification metric instead of pure visualization. The FSS of the numerical experiments KF_WSM6, KF_Lin, KF_Thompson, and KF_Morrison for the individual cyclones and all cyclones combined are illustrated in figure 14. Figure 14 shows that the Thompson scheme has higher FSS than the remaining schemes, whereas the Morrison scheme has the next highest FSS. This strengthens the result obtained by the visual comparison. From the above results, it is evident that the Thompson scheme is the best MP scheme for simulating the reflectivity.

To understand the differences in the reflectivity estimation by each MP scheme, the contribution of hydrometeors, namely rain, snow, and graupel at altitudes of 3 km and 8 km for cyclone Fani, are studied and presented in figure 15. The figure shows that rain is the dominating hydrometeor at an altitude of 3 km, whereas the snow and graupel dominate at an altitude of 8 km, strengthening the earlier statement. The Lin scheme produces a huge amount of rain throughout the inner and outer rain bands, whereas the remaining schemes produce rain only at the inner rain bands. The WSM6, Thompson, and Morrison schemes show no traces of snow and graupel at 3 km level. However, the Lin scheme produces considerable amounts of snow and graupel at 3 km, which is not very common at this level. A close observation of the contribution of the hydrometeors at an altitude of 8 km reveals that the contribution of snow dominates in the inner rain bands and around the eyewall for WSM6, Thompson, and Morrison schemes. In contrast, for the Lin scheme, the contribution of graupel dominates in the inner rain band and around the eyewall, and the presence of snow is seen all around the cyclone core region, i.e., around the inner rainband. For the WSM6 scheme, close observation of figures 12(A2) and 15(a5, a6) show that the cells with reflectivities more than 30 dBZ are caused by the presence of graupel but are very few in number. At the same time, the reflectivities caused by the snow are also considerably high. For the Lin scheme, figures 12(A3) and 15(b5, b6) show that the dominant contributor of the reflectivity is graupel, whereas the presence of snow around the inner rain band did not produce any

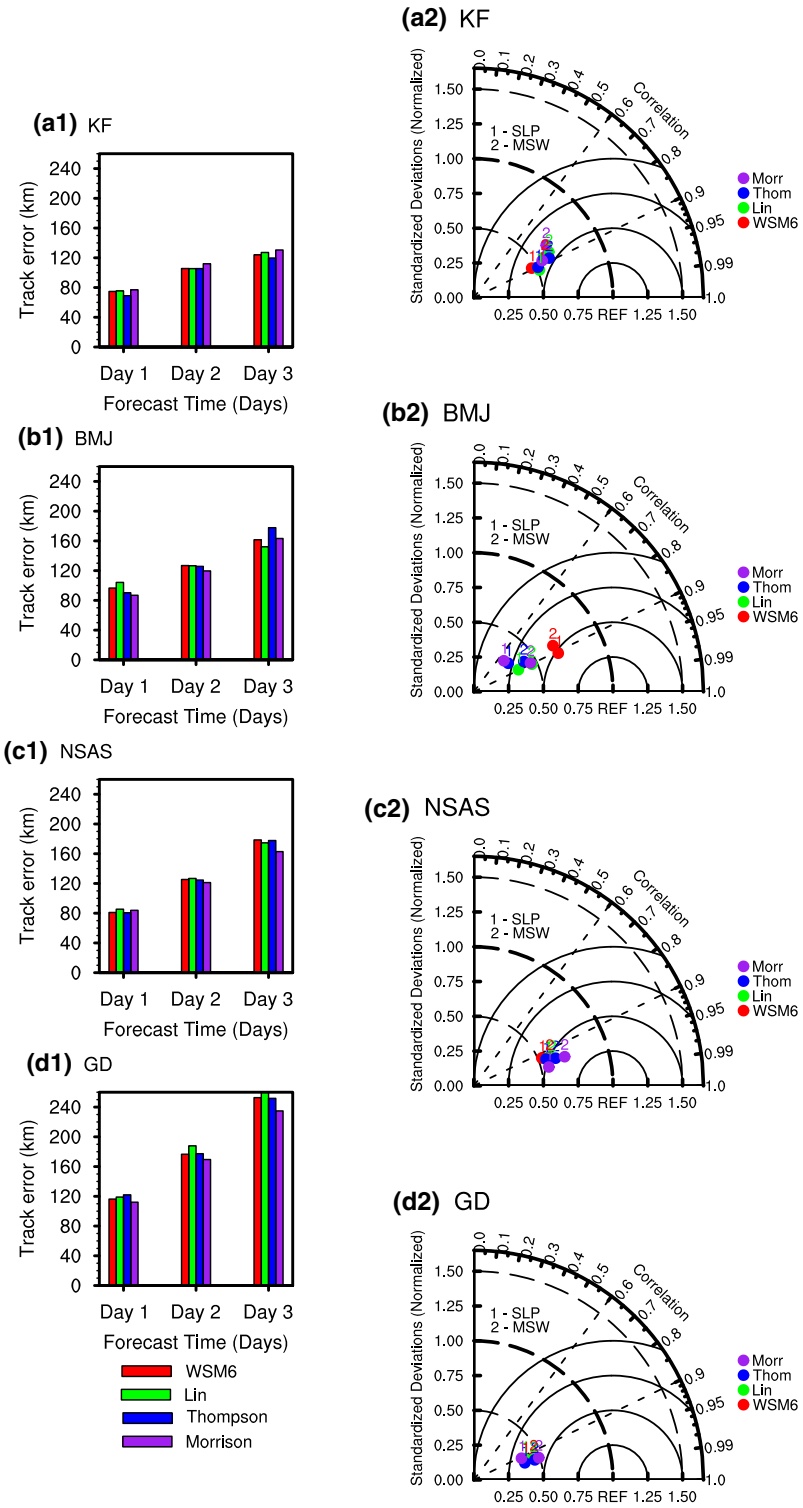

Figure 8. The composited (seven TCs) statistics of cyclone track error, CSLP, and MSW comparison between different numerical experiments. Each subfigure presents the statistics of numerical experiments corresponding to one CP scheme in combination with four MP schemes. (**a1–d1**) present the composited daily track errors. (**a2–d2**) present the composited normalized statistics of CSLP and MSW using Taylor diagrams.

reflectivities greater than 17 dBZ (below which the simulated reflectivities are discarded, as explained earlier). For the Thompson scheme, though snow is the dominating hydrometeor, it did not produce reflectivities greater than 17 dBZ, except at the inner rainband and the eyewall, which is found by

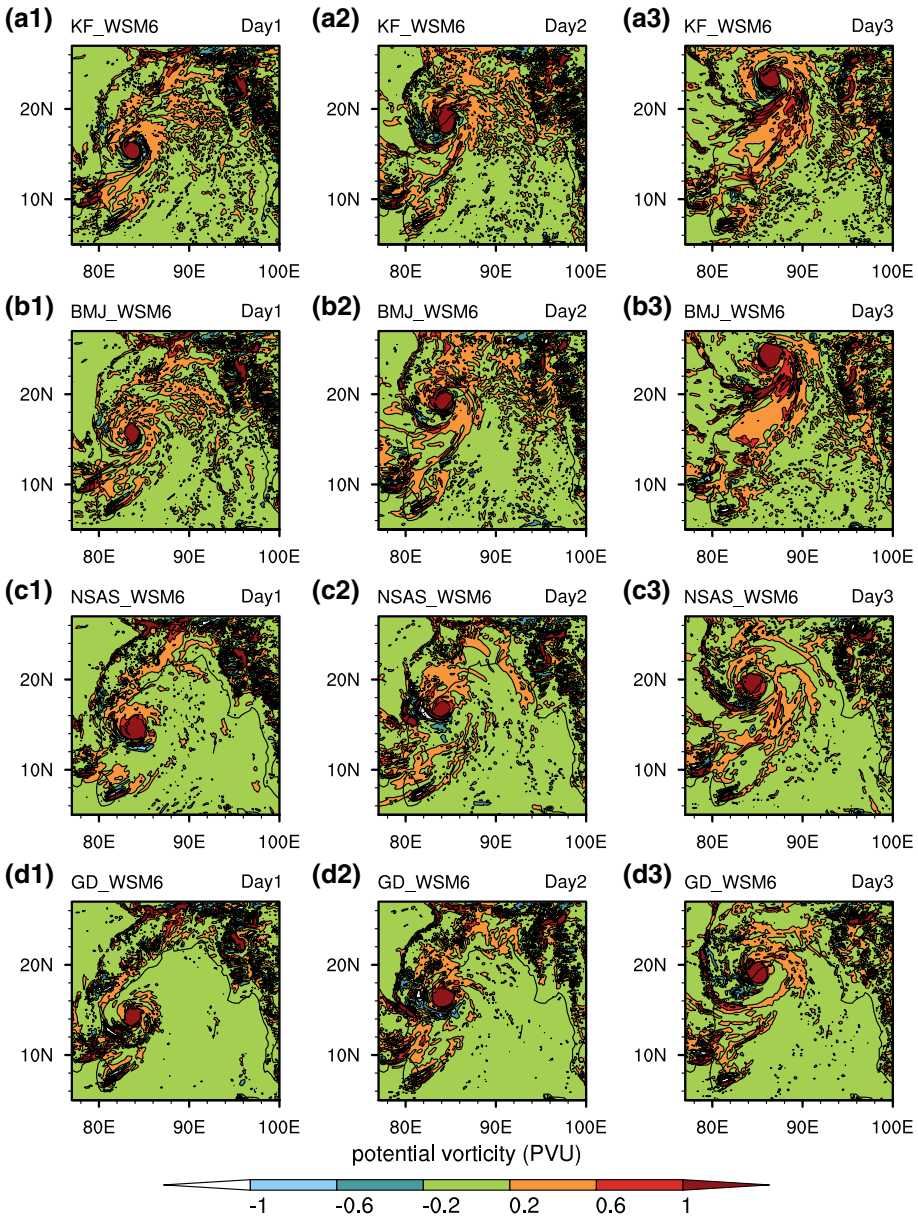

Figure 9. The low troposphere (950 hPa) potential vorticity field of cyclone Fani simulated using (**a1–a3**) KF_WSM6, (**b1–b3**) BMJ_WSM6, (**c1–c3**) NSAS_WSM6, and (**d1–d3**) GD_WSM6 experiments. Figure (**a1–d1**) shows the potential vorticity field at the end of first day, (**a2–d2**) second day, and (**a3–d3**) third day.

observing figures 12(A4) and 15(c5, c6), and the presence of graupel at very confined locations produce reflectivities greater than 30 dBZ. For the Morrison scheme, figures 12(A5) and 15(d5, d6) show that the contribution of graupel is very minimal, but produces strong reflectivities, and dominant hydrometeor snow produces moderate reflectivities.

To further demonstrate the differences in reflectivity between the MP scheme and the role of hydrometeors in reflectivity estimation, the vertical profiles of reflectivities and the hydrometeor mixing ratios are plotted in figure 16, for cyclone Fani. The black line shows the observed KuPR reflectivity, the reflectivities contributed by rain, snow, and graupel are shown by blue, brown, and pink lines, respectively, and the simulated reflectivity, which is the sum of contributions of each hydrometeor, is shown by the green line. The vertical profiles of hydrometeors are shown in the second column. The results show that the observed reflectivity profile consists of constant reflectivity till the melting layer (approximately at 5 km), a sharp increase in reflectivity just above the melting

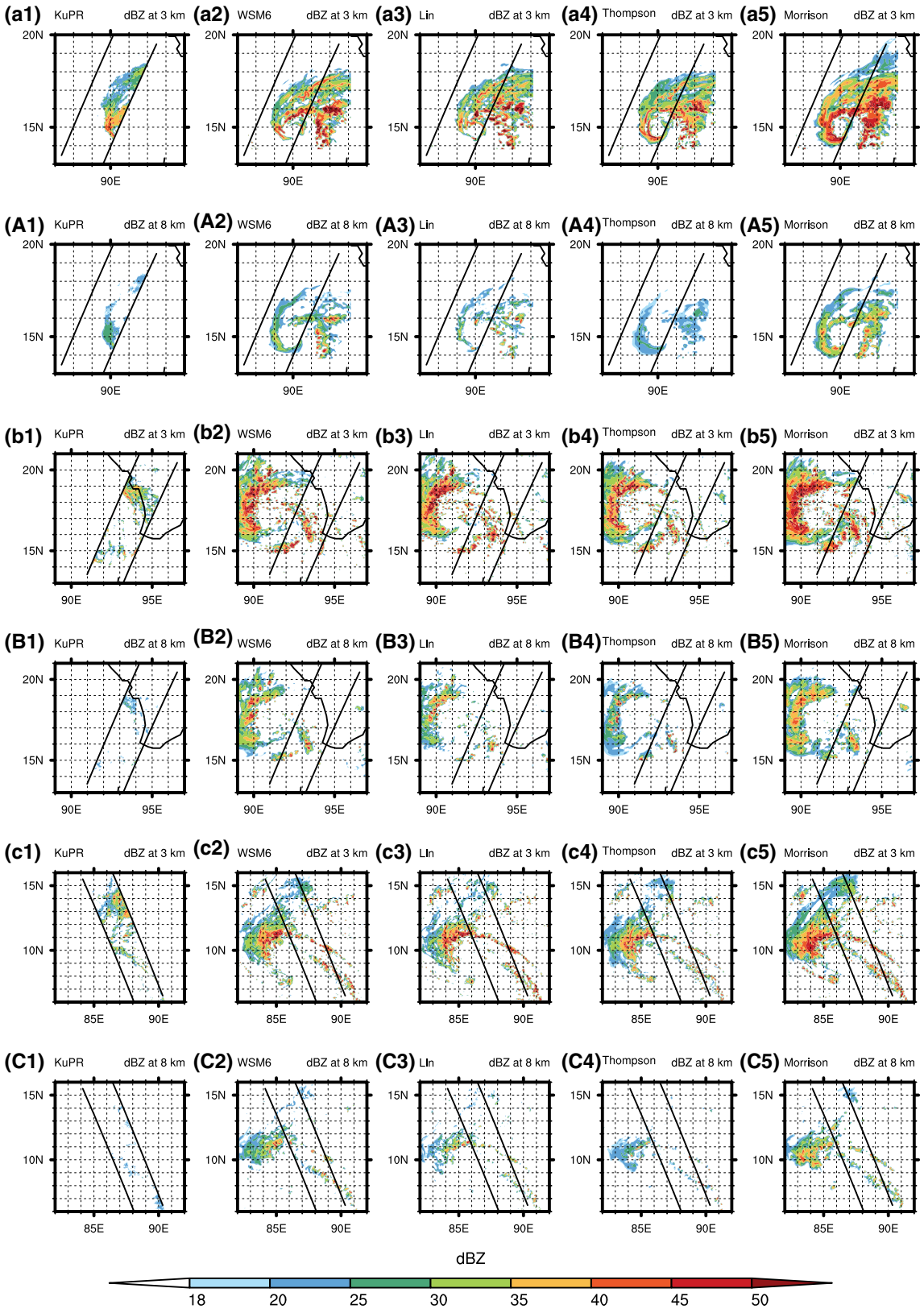

Figure 10. (**a1–C1**) The GPM-KuPR reflectivity compared with the WRF simulated reflectivity using the experiments (**a2–C2**) KF_WSM6, (**a3–C3**) KF_Lin, (**a4–C4**) KF_Thompson, and (**a5–C5**) KF_Morrison experiments, (**a1–A5**) for cyclone Maarutha, (**b1–B5**) for cyclone Mora, and (**c1–C5**) for cyclone Phethai. Figure (**a1–a5**) shows the reflectivities at 3 km and (**A1–A5**) show the reflectivities at 8 km altitude for cyclone Maarutha. The remaining rows show a similar naming for cyclones Mora and Phethai.

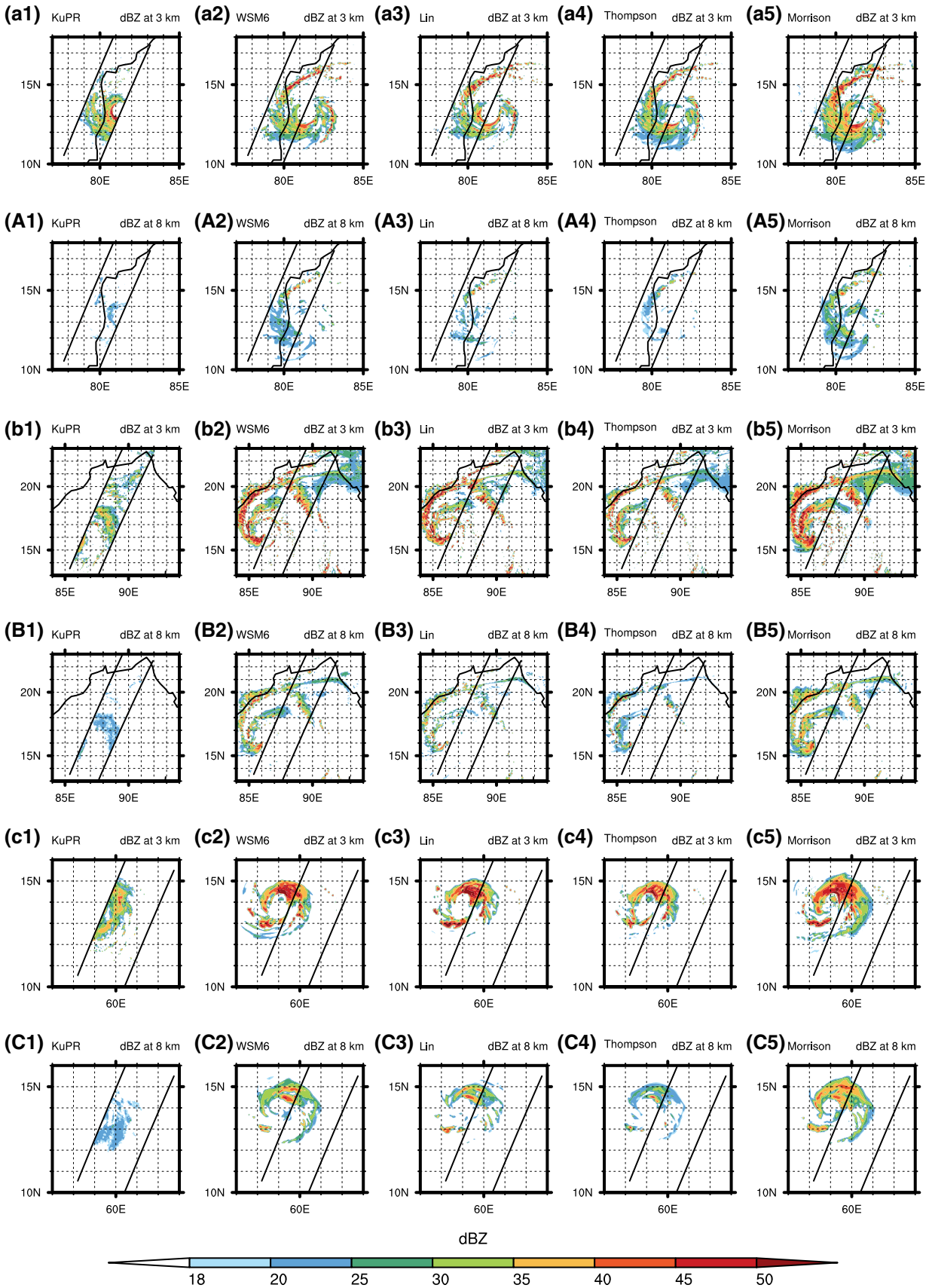

Figure 11. (**a1–C1**) The GPM-KuPR reflectivity compared with the WRF simulated reflectivity using the experiments (**a2–C2**) KF_WSM6, (**a3–C3**) KF_Lin, (**a4–C4**) KF_Thompson, and (**a5–C5**) KF_Morrison experiments, (**a1–A5**) for cyclone Vardah, (**b1–B5**) for cyclone Titli, and (**c1–C5**) for cyclone Chapala. Figure (**a1–a5**) shows the reflectivities at 3 km and (**A1–A5**) show the reflectivities at 8 km altitude for cyclone Vardah. The remaining rows show a similar naming for cyclones Titli and Chapala.

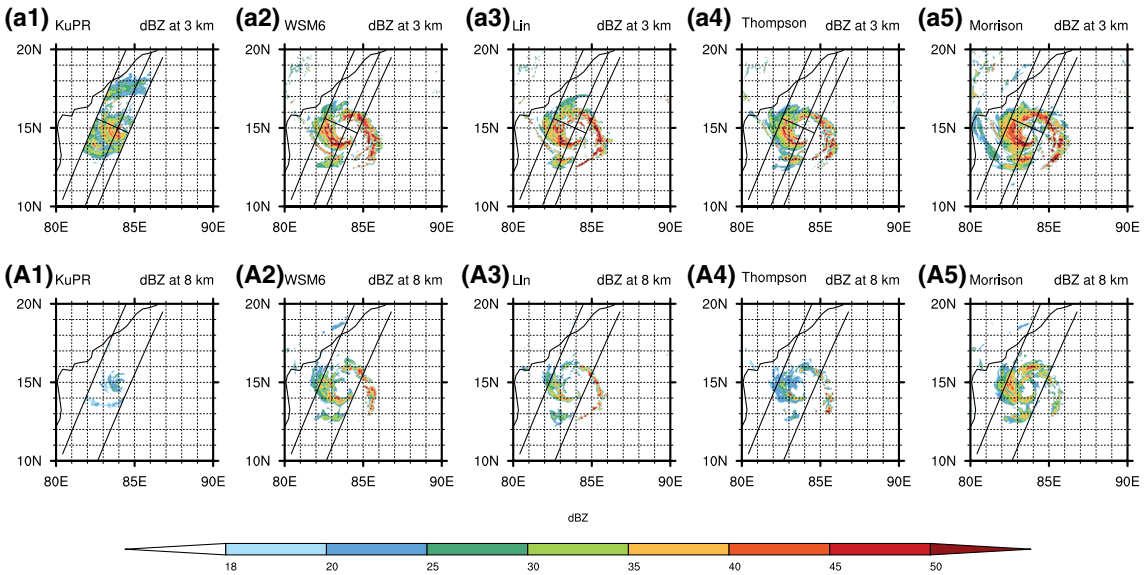

Figure 12. (**a1–A1**) The GPM-KuPR reflectivity compared with the WRF simulated reflectivity using the experiments (**a2–A2**) KF_WSM6, (**a3–A3**) KF_Lin, (**a4–A4**) KF_Thompson, and (**a5–A5**) KF_Morrison experiments, for cyclone Fani. Figure (**a1–a5**) shows the reflectivities at 3 km and (**A1–A5**) show the reflectivities at 8 km altitude.

layer indicating the presence of brightband and a sharp decrease in the reflectivity thereafter. The presence of brightband is a common feature of stratiform clouds (Sun *et al.* 2020). The CR-SIM software is not designed to produce any brightband and is not so observed in the simulated profile. Due to the similarity in the drop size distribution of rain species in the MP schemes, the reflectivity profiles below the melting layer are also very similar to variations in their intensities attributed to the differences in their rainwater mixing ratios. The WSM6 and Lin schemes show a resemblance in their reflectivity profile below the melting layer and the corresponding rainwater mixing ratio, which can be attributed to the same drop size distribution of rainwater in both schemes. In contrast, the rainwater drop size distribution in the Thompson and Morrison schemes are different, which leads to a lesser intense reflectivity corresponding to the rainwater. As stated earlier, the major difference in the MP schemes comes in the drop size distributions of snow and graupel, which can be clearly seen in the vertical profiles of reflectivity and mixing ratios. A major observation from the figures is that the presence of graupel greatly increases the reflectivity. The drop size distribution of graupel in WSM6 and Lin are also the same, which leads to a similar mixing ratio and reflectivity profiles of graupel for these two schemes. Due to the difference in the snow size distribution, the WSM6 produces a greater amount of snow compared to the Lin scheme, which ultimately leads to the differences in their reflectivity profiles. The Morrison scheme, which calculates the reflectivity based on the prognostic number concentration, produces similar snow and graupel reflectively profiles. The Thompson scheme, specially designed for the snow species, produces an enormous amount of snow mixing ratio, but its reflectivity profile is cut short, which is attributed to its drop size distribution. Among the four MP schemes, only the Thompson scheme produced a drastic decrease in reflectivity just above the melting layer, which is mainly attributed to the lesser intense graupel profile. Figure 16 shows that the Thompson scheme produced a relatively similar reflectivity profile to that of the KuPR profile compared to the remaining schemes. These findings strengthen the argument that the Thompson scheme is the best among all the schemes considered in this study.

3.3 *Performance comparison of the best set of schemes with a random set of schemes*

There exists a need to verify the robustness of the best set of schemes obtained from this study. Therefore, cyclone Bulbul is simulated using the best set and a random set of schemes. The comparison statistics such as track, the time evolution of SLP and MSW, Taylor plots of SLP and MSW, daily track error, and FSS are presented in figure 17. The track obtained from the best set of

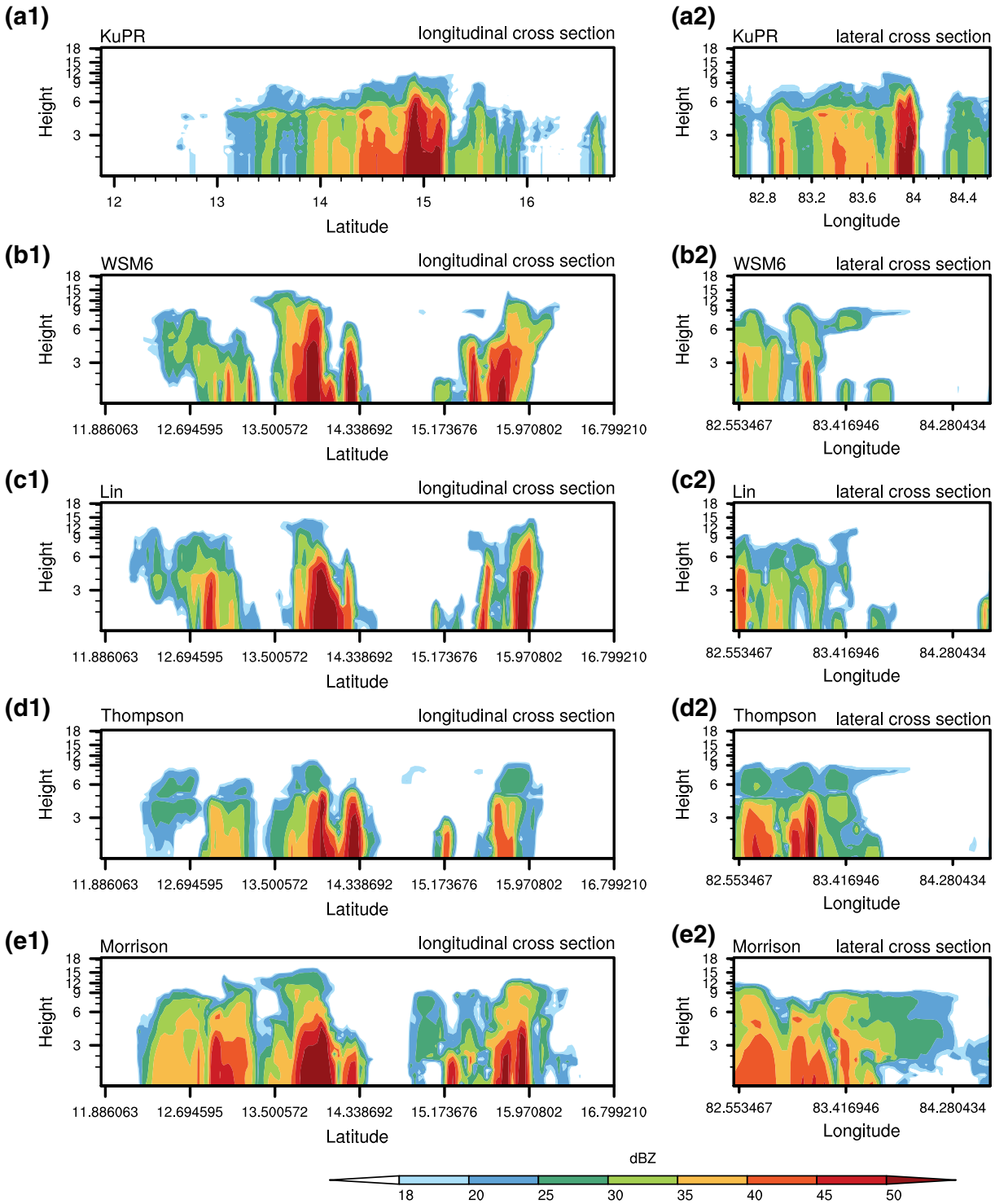

Figure 13. Vertical cross-section of simulated reflectivity compared with the GPM reflectivity for cyclone Fani, along the longitudinal and lateral lines that are shown in figure 12(**a1–a5**). (**a1–a2**) correspond GPM-KuPR reflectivity, (**b1–b2**) simulated reflectivity using the experiments KF_WSM6, (**c1–c2**) KF_Lin, (**d1–d2**) KF_Thompson, and (**e1–e2**) KF_Morrison experiments.

schemes closely followed the observed track till the end of the second day and deviated thereafter, whereas the track obtained from the random set deviated from the observed track at the end of the first day. The same trend can be found in the track error figure 17(e) which shows the best set having the least track error. The best set simulated a minimum SLP of 970 hPa beyond the observed minimum SLP and closely followed the intensity evolution. However, the random set failed to reach

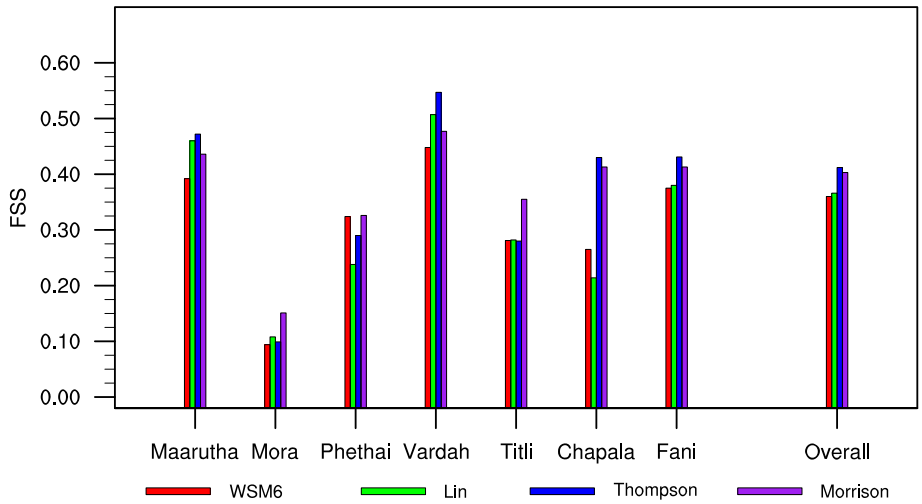

Figure 14. The fraction skill scores of the individual cyclones and all cyclones combined simulated by the experiments KF_WSM6, KF_Lin, KF_Thompson, and KF_Morrison.

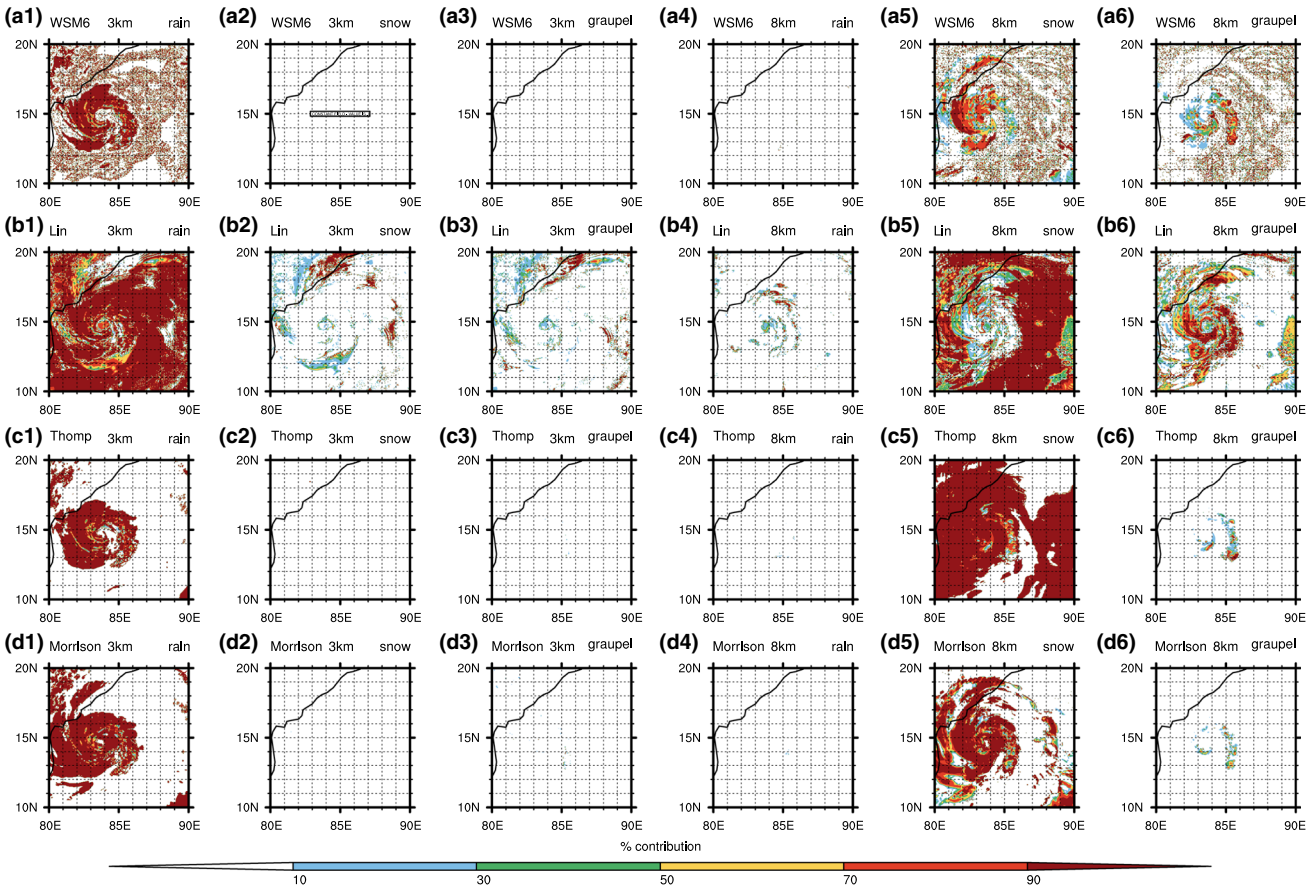

Figure 15. Contribution of simulated hydrometeor mixing ratios at two levels for cyclone Fani, using the experiments (**a1–a6**) KF_WSM6, (**b1–b6**) KF_Lin, (**c1–c6**) KF_Thompson, and (**d1–d6**) KF_Morrison. Figures (**a1–d1**) correspond to rain, (**a2–d2**) correspond to snow, and (**a3–d3**) correspond to graupel, at 3 km altitude. Similarly, next three columns correspond to rain, snow, and graupel at 8 km altitude.

intensity beyond 30 m/s and the minimum SLP of 985 hPa. The Taylor statistics shown in figure 17(d) reveals that the best set performed better than the random set with the highest correlation and the least RMSE value. A comparison of reflectivities at 3 km and 8 km altitudes

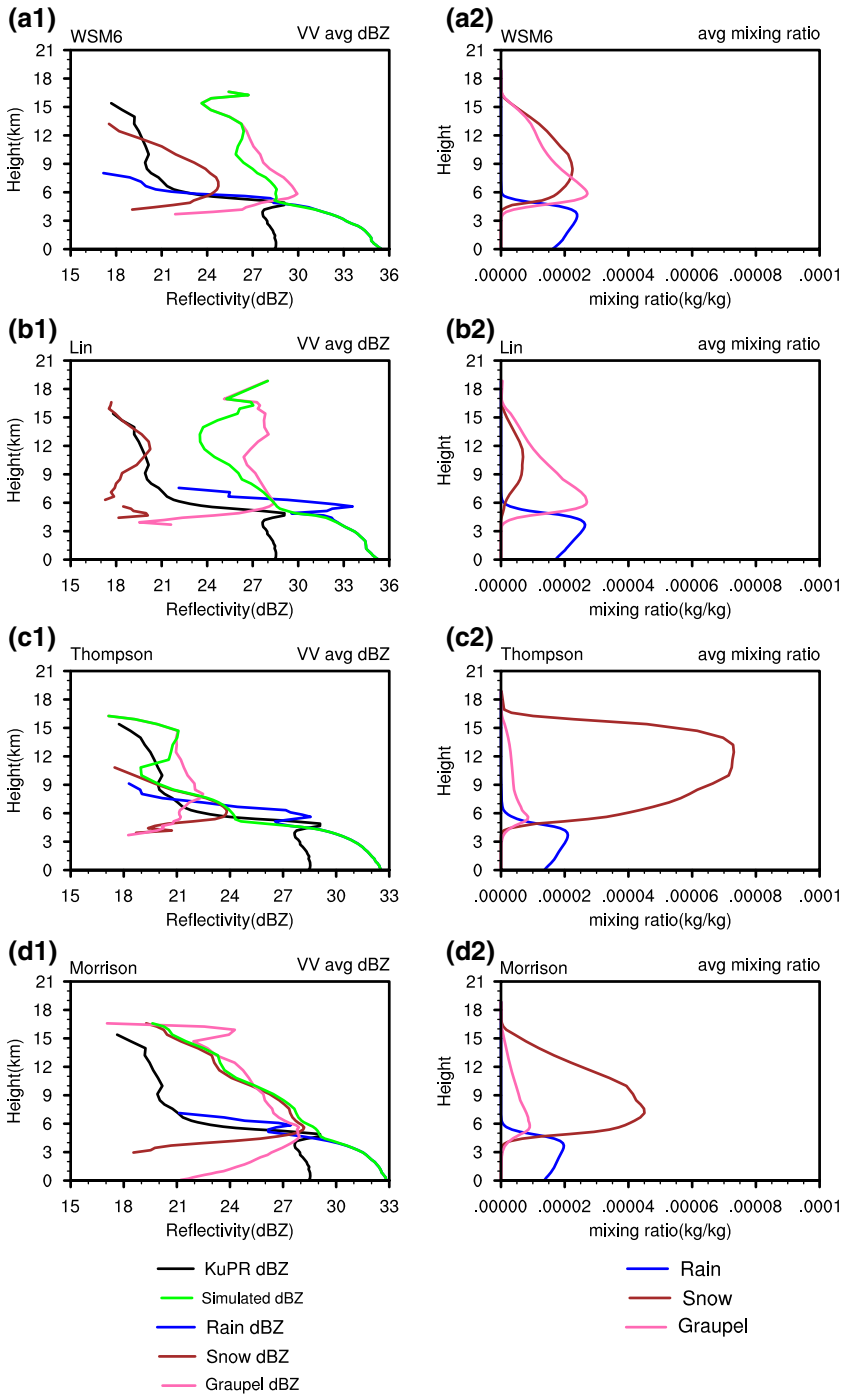

Figure 16. Vertical profiles of (**a1–d1**) reflectivities and (**a2–d2**) hydrometeor mixing ratios for cyclone Fani, using the experiments (**a1–a2**) KF_WSM6, (**b1–b2**) KF_Lin, (**c1–c2**) KF_Thompson, and (**d1–d2**) KF_Morrison. In the first column, the black line shows the observed GPM-KuPR reflectivity profile, the green line shows simulated reflectivity profile, and the reflectivities contributed by the hydrometeors rain, and graupel are represented by blue, brown, and pink lines, respectively. Correspondingly, in the second column, the vertical profiles of mixing ratios of rain, snow, and graupel are represented by blue, brown, and pink lines, respectively.

(figures not shown) shows that the best set reproduces similar intensities of GPM-KuPR reflectivity. In contrast, the random set overestimates the intensities and simulates more convective cells at both altitudes. The FSS comparison, shown in figure 17(f), strengthens the results, with the best set having a higher FSS value than the random set. These results show that the

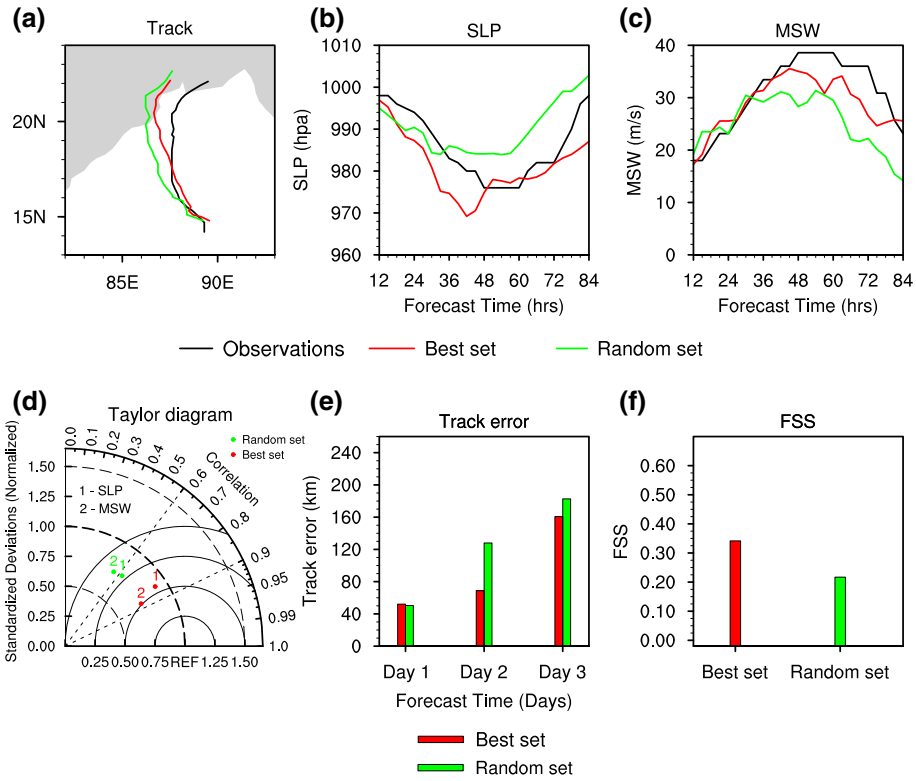

Figure 17. Comparison statistics of cyclone Bulbul using the best and the random set of schemes: (**a**) track, (**b**) time evolution of SLP, (**c**) time evolution of MSW, (**d**) Taylor statistics of SLP and MSW, (**e**) daily track error, and (**f**) FSS comparison.

best set performs better than the random set in every aspect. These results thus verify the performance of the best set of schemes obtained from this study.

4. Conclusions

The goal of the present study was to determine the best combination of cumulus and microphysics parameterization schemes for tropical cyclones. For this purpose, seven tropical cyclones: Maarutha, Mora, Phethai, Vardah, Titli, Chapala, and Fani, were simulated using the WRF model, with the combination of four microphysics schemes: WSM6, Purdue Lin, Thompson, and Morrison, and four cumulus physics schemes: KF, BMJ, NSAS, and GD. The model simulated track and intensity were validated against the IMD observations. The results showed that the KF scheme, combined with all MP schemes, had predicted the cyclone track more accurately than other schemes, whereas the MP schemes have a negligible impact on track prediction. A qualitative analysis conducted using the upper-level steering flows revealed that the KF scheme simulated strong upper-level anticyclonic circulation, which governed the cyclone movement. Among the CP schemes, the NSAS scheme predicted the cyclone intensity closest to the observations whereas the KF scheme found as the second best scheme. The KF scheme was found to simulate cyclones with high intensities, which was attributed to the simulation of more localized, small-scale potential vorticity disturbances. A further study was conducted to identify the best MP scheme in simulating the reflectivity using the GPM-KuPR radar data. The numerical experiments with the KF cumulus scheme were considered for the microphysics sensitivity study. The CR-SIM software was modified and used to calculate the simulated reflectivities from the model output. The simulated reflectivities were validated against the GPM-KuPR reflectivities. The results showed that the Thompson scheme had captured the intensities of the cyclones accurately with similar vertical profiles to that of the observed GPM-KuPR profile, compared to other MP schemes. This study identified the KF and Thompson as the best CP and MP schemes, respectively, for tropical cyclones simulations. The robustness of the best schemes was finally validated by simulating cyclone Bulbul, and it was found that the best set of schemes obtained from this study performed better than the random set of schemes.

Acknowledgements

The authors are thankful to the international WRF community for their tremendous efforts in developing the WRF model and supporting us through providing the model. The model simulations are performed on Aqua High-Performance Computing (HPC) system at the Indian Institute of Technology Madras, Chennai, India. The figures are plotted using the python language and NCAR Command Language (NCL). The authors would like to thank the 'Centre of Excellence (CoE) in climate change impact on coastal infrastructure and the adaptation strategies' for their suggestions. Department of Science and Technology is funding the research grant DST/CCP/CoE/141/2018(C) for this project (CIE1819265DSTXSACI) under SPLICE – Climate Change Programme.

Author statement

Harish Baki and Sandeep Chinta conceptualized the study, designed the methodology, performed the formal analysis and edited the draft of the paper. Harish Baki performed the investigation and prepared the original draft. C Balaji and Balaji Srinivasan provided critical revisions for the manuscript and supervised the work.

Appendix

A1. *Drop size distributions of hydrometeors in the Lin scheme*

The Purdue Lin scheme adopted classical exponential drop size distribution for hydrometeors rain, snow, and graupel as:

$$n(D) = N_0 e^{-\lambda D} dD \quad \text{in m}^{-3}.$$

Here, $n(D)$ is the drop size distribution as a function of the diameter D, dD is the differential diameter, N_0 is the intercept parameter, and λ is the slope parameter. The intercept and slope parameter values will vary for different hydrometeors.

A1.1 *Rain*

$$\begin{aligned} n_R(D) &= N_{0R} e^{-\lambda D} dD \quad \text{in m}^{-3} \\ N_{0R} &= 8 \times 10^6 \quad \text{in m}^{-4} \\ \lambda_R &= \left(\frac{\pi \rho_R N_{0R}}{\rho_{\text{dair}} Q_R}\right)^{\frac{1}{4}} \quad \text{in m}^{-1} \\ \rho_R &= 1000 \ \text{kg/m}^3. \end{aligned}$$

A1.2 *Snow*

$$\begin{aligned} n_S(D) &= N_{0S} e^{-\lambda D} dD \quad \text{in m}^{-3} \\ N_{0S} &= 3 \times 10^6 \quad \text{in m}^{-4} \\ \lambda_S &= \left(\frac{\pi \rho_S N_{0S}}{\rho_{\text{dair}} Q_S}\right)^{\frac{1}{4}} \quad \text{in m}^{-1} \\ \rho_S &= 100 \ \text{kg/m}^3. \end{aligned}$$

A1.3 *Graupel*

$$\begin{aligned} n_G(D) &= N_{0G} e^{-\lambda D} dD \quad \text{in m}^{-3} \\ N_{0G} &= 4 \times 10^6 \quad \text{in m}^{-4} \\ \lambda_G &= \left(\frac{\pi \rho_G N_{0G}}{\rho_{\text{dair}} Q_G}\right)^{\frac{1}{4}} \quad \text{in m}^{-1} \\ \rho_G &= 917 \ \text{kg/m}^3. \end{aligned}$$

In the above equations, Q_R, Q_S, Q_G are the mixing ratios (in kg/kg) of the hydrometeors rain, snow, and graupel, ρ_R, ρ_S, ρ_G are the densities, and ρ_{dair} is the dry air density (in kg/m^3).

A2. *Drop size distributions of hydrometeors in the WSM6 scheme*

The drop size distributions of the hydrometeors adopted in the WSM6 scheme are based on the Lin scheme, and thus follow the same exponential distribution, with a little modification adopted for snow.

A2.1 *Rain*

$$\begin{aligned} n_R(D) &= N_{0R} e^{-\lambda D} dD \quad \text{in m}^{-3} \\ N_{0R} &= 8 \times 10^6 \quad \text{in m}^{-4} \\ \lambda_R &= \left(\frac{\pi \rho_R N_{0R}}{\rho_{\text{dair}} Q_R}\right)^{\frac{1}{4}} \quad \text{in m}^{-1} \\ \rho_R &= 1000 \ \text{kg/m}^3. \end{aligned}$$

A2.2 *Snow*

$$\begin{aligned} n_S(D) &= N_{0S} e^{-\lambda D} dD \quad \text{in m}^{-3} \\ N_{0S} &= 2 \times 10^6 \times e^{0.12(T - T_0)} \quad \text{in m}^{-4} \\ \lambda_S &= \left(\frac{\pi \rho_S N_{0S}}{\rho_{\text{dair}} Q_S}\right)^{\frac{1}{4}} \quad \text{in m}^{-1} \\ \rho_S &= 100 \ \text{kg/m}^3. \end{aligned}$$

Here, T is the temperature (K) and T_0 is the reference temperature (273.16 K).

A2.3 *Graupel*

$$n_G(D) = N_{0G} e^{-\lambda D} dD \quad \text{in m}^{-3}$$
$$N_{0G} = 4 \times 10^6 \quad \text{in m}^{-4}$$
$$\lambda_G = \left(\frac{\pi \rho_G N_{0G}}{\rho_{\text{dair}} Q_G}\right)^{\frac{1}{4}} \quad \text{in m}^{-1}$$
$$\rho_G = 500 \text{ kg/m}^3.$$

A3. *Drop size distributions of hydrometeors in the Thompson scheme*

The Thompson scheme assumes generalized gamma distribution for each hydrometeor (except for snow) as:

$$n(D) = \frac{N_t}{\Gamma(\mu+1)} \lambda^{\mu+1} D^{\mu} e^{-\lambda D} dD$$
$$\lambda = \left[\frac{\Gamma(1+\mu+b_m)}{\Gamma(1+\mu)} \frac{a_m N_x}{Q_x}\right]^{1/b_m}$$
$$N_t = N_x \rho_{\text{dair}}.$$

Here, N_t is the total number concentration, N_x is the prognostic number concentration (in 1/kg) of hydrometeor x, Q_x is the mixing ratio of hydrometeor x, a_m and b_m are the constant and exponents of mass-size relationship, Γ is the gamma function, and μ is the shape parameter. When $\mu = 0$, the distribution becomes the classical exponential distribution. In the Thompson scheme, along with the mixing ratios, the number concentrations of rain and ice particles are also simulated. Thus, the scheme is known to be a double-moment scheme. Further information can be found at Oue *et al.* (2019).

A3.1 *Rain*

For rain particles, the shape parameter is 0. Thus, the drop size distributions becomes classical exponential distribution. The scheme uses the model simulated prognostic rain number concentration in the distribution.

$$n_R(D) = N_t e^{-\lambda D} dD \text{ in m}^{-3}$$
$$\lambda_R = \left[\frac{\Gamma(1+b_m)}{\Gamma(1)} \frac{a_m N_R}{Q_R}\right]^{1/b_m} \text{ in m}^{-1}$$

with $a_m = \frac{\pi \rho_R}{6}$, $b_m = 3$, the distribution reduces to

$$\lambda_R = \left(\frac{\pi \rho_R N_R}{Q_R}\right)^{\frac{1}{3}} \text{ in m}^{-1}$$
$$N_t = N_R \rho_{\text{dair}}$$
$$\rho_R = 1000 \text{ kg/m}^3.$$

Here, N_R is the number concentration (in 1/kg).

A3.2 *Snow*

The Thompson scheme specially build for snow. Unlike the exponential or generalized gamma distribution, it follows the combination of both.

$$n_S(D) = \frac{\mathcal{M}_2^4}{\mathcal{M}_3^3}\left[K_0 e^{-\frac{\mathcal{M}_2}{\mathcal{M}_3}\wedge_0 D} + K_1 \left(\frac{\mathcal{M}_2}{\mathcal{M}_3} D\right)^{\mu_s} e^{-\frac{\mathcal{M}_2}{\mathcal{M}_3}\wedge_1 D}\right]$$
in m^{-3}

$$\mathcal{M}_n = \int D^n N(D) dD$$
is the *nth* moment size distribution

$$\mathcal{M}_n = a(n, T_c) \mathcal{M}_2^{b(n,T_c)}$$
$$\log(a, T_c) = 5.065339 - 0.062659 T_c - 3.032362 n + 0.029469 T_c n - 0.000285 T_c^2 + 0.312550 n^2 + 0.000204 T_c^2 n + 0.003199 T_c n^2 + 0.000000 T_c^3 - 0.015952 n^3$$
$$b(n, T_c) = 0.476221 - 0.015896 T_c + 0.165977 n + 0.007468 T_c n - 0.000141 T_c^2 + 0.060366 n^2 + 0.000079 T_c^2 n + 0.000594 T_c n^2 + 0.000000 T_c^3 - 0.003577 n^3$$

where $K_0 = 490.6, K_1 = 17.56, \wedge_0 = 20.78, \wedge_1 = 3.29, \mu_s = 0.6357$, and T_c is the air temperature in °C, $\rho_S = 100 \text{ kg/m}^3$.

A3.3 *Graupel*

For graupel also, the shape parameter is 0.

$$n_G(D) = N_{0G} e^{-\lambda D} dD \text{ in m}^{-3}$$
$$N_{0G} = \max\left[10^4, \min\left(\frac{200}{Q_g}, 5 \times 10^6\right)\right] \text{ in m}^{-4}$$
$$\lambda_G = \left(\frac{\pi \rho_G N_{0G}}{\rho Q_G}\right)^{\frac{1}{4}} \text{ in m}^{-1}$$
$$\rho_G = 500 \text{ kg/m}^3.$$

A4. *Drop size distributions of hydrometeors in the Morrison double moment scheme*

The Morrison scheme also adopted generalized gamma distribution for every hydrometeor. The scheme simulated number concentrations for all the hydrometeors, except cloud water. The shape parameter μ is considered zero for rain, snow, and graupel. Thus, the generalized gamma distribution simplified to an exponential distribution, with $N_t\lambda$ being considered as intercept. In addition, the constant and exponents of mass-diameter parameters are $a_m = \frac{\pi\rho_x}{6}$ and $b_m = 3$.

A4.1 *Rain*

$$n_R(D) = N_{0R}e^{-\lambda D}dD \quad \text{in m}^{-3}$$
$$N_{0R} = N_t\lambda = N_R\rho_{\text{dair}}\lambda \quad \text{in m}^{-4}$$
$$\lambda_R = \left[\frac{\Gamma(1+b_m)}{\Gamma(1)}\frac{a_m N_R}{Q_R}\right]^{1/b_m} \quad \text{in m}^{-1}$$
$$\lambda_R = \left(\frac{\pi\rho_R N_R}{Q_R}\right)^{\frac{1}{3}} \quad \text{in m}^{-1}$$
$$\rho_R = 997 \text{ kg/m}^3.$$

A4.2 *Snow*

$$n_S(D) = N_{0S}e^{-\lambda D}dD \quad \text{in m}^{-3}$$
$$N_{0S} = N_S\rho_{\text{dair}}\lambda \quad \text{in m}^{-4}$$
$$\lambda_S = \left(\frac{\pi\rho_S N_S}{Q_S}\right)^{\frac{1}{3}} \quad \text{in m}^{-1}$$
$$\rho_S = 100 \text{ kg/m}^3.$$

A4.3 *Graupel*

$$n_G(D) = N_{0S}e^{-\lambda D}dD \quad \text{in m}^{-3}$$
$$N_{0S} = N_S\rho_{\bar{\text{dair}}}\lambda \quad \text{in m}^{-4}$$
$$\lambda_S = \left(\frac{\pi\rho_G N_S}{Q_S}\right)^{\frac{1}{3}} \quad \text{in m}^{-1}$$
$$\rho_G = 400 \text{ kg/m}^3.$$

In the above equations, N_R, N_S, N_G are the number concentrations (in 1/kg) for rain, snow, and graupel, respectively.

References

Alam M M, Hossain M A and Shafee S 2003 Frequency of Bay of Bengal cyclonic storms and depressions crossing different coastal zones; *Int. J. Climatol.* **23(9)** 1119–1125.

Balaguru K, Taraphdar S, Leung L R and Foltz G R 2014 Increase in the intensity of post-monsoon Bay of Bengal tropical cyclones; *Geophys. Res. Lett.* **41(10)** 3594–3601.

Beljaars A C M 2004 The parameterization of surface fluxes in large-scale models under free convection; *Quart. J. Roy. Meteor. Soc.* **121(522)** 255–270.

Chandrasekar R and Balaji C 2012 Sensitivity of tropical cyclone Jal simulations to physics parameterizations; *J. Earth Syst. Sci.* **121(4)** 923–946.

Chen S H and Sun W Y 2002 A one-dimensional time dependent cloud model; *J. Meteorol. Soc. Japan* **80(1)** 99–118.

Choudhury D and Das S 2017 The sensitivity to the micro-physical schemes on the skill of forecasting the track and intensity of tropical cyclones using WRF-ARW model; *J. Earth Syst. Sci.* **126(4)** 57.

Elsberry R L 2014 Advances in research and forecasting of tropical cyclones from 1963–2013; *Asia-Pacific J. Atmos. Sci.* **50(1)** 3–16.

Franklin C N, Holland G J and May P T 2005 Sensitivity of tropical cyclone rainbands to ice-phase microphysics; *Mon. Weather Rev.* **133(8)** 2473–2493.

Grell G A and Dévényi D 2002 A generalized approach to parameterizing convection combining ensemble and data assimilation techniques; *Geophys. Res. Lett.* **29(14)**.

Grell G A and Freitas S R *et al.* 2014 A scale and aerosol aware stochastic convective parameterization for weather and air quality modeling; *Atmos. Chem. Phys.* **14(10)** 5233–5250.

Han J and Pan H L 2011 Revision of convection and vertical diffusion schemes in the NCEP global forecast System; *Weather Forecast.* **26(4)** 520–533.

Hong S Y, Dudhia J and Chen S H 2004 A revised approach to ice microphysical processes for the bulk parameterization of clouds and precipitation; *Mon. Weather Rev.* **132(1)** 103–120.

Hong S Y, Noh Y and Dudhia J 2006 A new vertical diffusion package with an explicit treatment of entrainment processes; *Mon. Weather Rev.* **134(9)** 2318–2341.

Hou A Y, Kakar R K, Neeck S, Azarbarzin A A, Kummerow C D, Kojima M, Oki R, Nakamura K and Iguchi T 2014 The global precipitation measurement mission; *Bull. Am. Meteorol. Soc.* **95(5)** 701–722.

Huang Y, Wang Y, Xue L, Wei X, Zhang L and Li H 2020 Comparison of three microphysics parameterization schemes in the WRF model for an extreme rainfall event in the coastal metropolitan city of Guangzhou, China; *Atmos. Res.* **240** 104939.

Iacono M J, Delamere J S, Mlawer E J, Shephard M W, Clough S A and Collins W D 2008 Radiative forcing by long-lived greenhouse gases: Calculations with the AER radiative transfer models; *J. Geophys. Res. Atmos.* **113(D13)**.

IMD 2015 Extremely Severe Cyclonic Storm, 'CHAPALA' over the Arabian Sea (28 October–4 November, 2015): A Report–India Meteorological Department, New Delhi.

IMD 2016 Very Severe Cyclonic Storm, 'Vardah' over the Bay of Bengal (06–13 December 2016): A Report – India Meteorological Department, New Delhi.

IMD 2017a Cyclonic Storm, 'Maarutha' over the Bay of Bengal (15–17 April 2017): A Report – India Meteorological Department, New Delhi.

IMD 2017b Severe Cyclonic Storm, 'Mora' over the Bay of Bengal (28–31 May 2017): A Report – India Meteorological Department, New Delhi.

IMD 2018a Severe Cyclonic Storm, 'P_{Hethai}' over southeast Bay of Bengal (13–18 December 2018): A Report – India Meteorological Department, New Delhi.

IMD 2018b Very Severe Cyclonic Storm 'Titli' over east central Bay of Bengal (08–13 October 2018): Summary – India Meteorological Department, New Delhi.

IMD 2019a Extremely Severe Cyclonic Storm 'F_{ani}' over east central equatorial Indian Ocean and adjoining southeast Bay of Bengal (26 April–04 May, 2019): Summary – India Meteorological Department, New Delhi.

IMD 2019b Very Severe Cyclonic Storm 'Bulbul' over the Bay of Bengal (05th–11th November 2019): Summary – India Meteorological Department, New Delhi.

Janjić Z I 1994 The step-mountain eta coordinate model: Further developments of the convection, viscous sublayer, and turbulence closure schemes; *Mon. Weather Rev.* **122(5)** 927–945.

Kain J S 2004 The Kain–Fritsch convective parameterization: An update; *J. Appl. Meteorol.* **43(1)** 170–181.

Kanase R D and Salvekar P 2015 Effect of physical parameterization schemes on track and intensity of cyclone LAILA using WRF model; *Asia-Pacific J. Atmos. Sci.* **51(3)** 205–227.

Koch S E, Ferrier B, Stoelinga M T, Szoke E, Weiss S J and Kain J S 2005 The use of simulated radar reflectivity fields in the diagnosis of mesoscale phenomena from high-resolution WRF model forecasts; In: Preprints, 11th Conf. on Mesoscale Processes, Albuquerque, NM, *Am. Meteorol. Soc.* J4J, **7** 1–9.

Kumar S and Bhat G 2016 Vertical profiles of radar reflectivity factor in intense convective clouds in the tropics; *J. Appl. Meteorol. Climatol.* **55(5)** 1277–1286.

Lim K S S and Hong S Y 2010 Development of an effective double-moment cloud microphysics scheme with prognostic cloud condensation nuclei (CCN) for weather and climate models; *Mon. Weather Rev.* **138(5)** 1587–1612.

Ma L M and Tan Z M 2009 Improving the behavior of the cumulus parameterization for tropical cyclone prediction: Convection trigger; *Atmos. Res.* **92(2)** 190–211.

Min K H, Choo S, Lee D and Lee G 2015 Evaluation of WRF cloud microphysics schemes using radar observations; *Weather Forecast.* **30(6)** 1571–1589.

Mishchenko M I and Travis L D 1998 Capabilities and limitations of a current FORTRAN implementation of the T-matrix method for randomly oriented, rotationally symmetric scatterers; *J. Quant. Spectrosc. Radiat. Transfer* **60(3)** 309–324.

Mlawer E J, Taubman S J, Brown P D, Iacono M J and Clough S A 1997 Radiative transfer for inhomogeneous atmospheres: RRTM, a validated correlated-k model for the longwave; *J. Geophys. Res. Atmos.* **102(D14)** 16,663–16,682.

Morrison H, Thompson G and Tatarskii V 2009 Impact of cloud microphysics on the development of trailing stratiform precipitation in a simulated squall line: Comparison of one-and two-moment schemes; *Mon. Weather Rev.* **137(3)** 991–1007.

Mukhopadhyay P, Taraphdar S and Goswami B 2011 Influence of moist processes on track and intensity forecast of cyclones over the North Indian ocean; *J. Geophys. Res. Atmos.* **116(D5)**.

Osuri K K, Mohanty U, Routray A, Kulkarni M A and Mohapatra M 2012 Customization of WRF-ARW model with physical parameterization schemes for the simulation of tropical cyclones over north Indian ocean; *Nat. Hazards* **63(3)** 1337–1359.

Oue M, Tatarevic A, Kollias P, Wang D, Yu K and Vogelmann A M 2019 The Cloud Resolving Model Radar Simulator (CR-SIM) Version 3.2: Description and Applications of a Virtual Observatory; *Geoscientific Model Development Discussions* **2019** 1–31, https://doi.org/10.5194/gmd-2019-207; https://www.geosci-model-dev-discuss.net/gmd-2019-207.

Pattanaik D and Rao Y R 2009 Track prediction of very severe cyclone 'Nargis' using high resolution weather research forecasting (wrf) model; *J. Earth Syst. Sci.* **118(4)** 309–329.

Pattanayak S, Mohanty U and Osuri K K 2012 Impact of parameterization of physical processes on simulation of track and intensity of tropical cyclone Nargis (2008) with WRF-NMM model; *Sci. World J.* **2012** 671437.

Pennelly C, Reuter G and Flesch T 2014 Verification of the wrf model for simulating heavy precipitation in Alberta; *Atmos. Res.* **135** 172–192.

Rao D V B, Srinivas D and Satyanarayana G C 2019 Trends in the genesis and landfall locations of tropical cyclones over the Bay of Bengal in the current global warming era; *J. Earth Syst. Sci.* **128(7)** 1–10.

Reddy P J, Sriram D, Gunthe S and Balaji C 2021 Impact of climate change on intense Bay of Bengal tropical cyclones of the post-monsoon season: A pseudo global warming approach; *Clim. Dyn.* **56(9)** 2855–2879.

Roberts N M and Lean H W 2008 Scale-selective verification of rainfall accumulations from high-resolution forecasts of convective events; *Mon. Weather Rev.* **136(1)** 78–97.

Rogers R F, Black M L, Chen S S and Black R A 2007 An evaluation of microphysics fields from mesoscale model simulations of tropical cyclones. Part I: Comparisons with observations; *J. Atmos. Sci.* **64(6)** 1811–1834.

Ryzhkov A, Pinsky M, Pokrovsky A and Khain A 2011 Polarimetric radar observation operator for a cloud model with spectral microphysics; *J. Appl. Meteorol. Climatol.* **50(4)** 873–894.

Sandeep C, Krishnamoorthy C and Balaji C 2018 Impact of cloud parameterization schemes on the simulation of cyclone Vardah using the WRF model; *Curr. Sci.* **115(6)**.

Skamarock W C, Klemp J B, Dudhia J, Gill D O, Barker D M, Wang W and Powers J G 2008 A description of the Advanced Research WRF version 3 NCAR Technical note-475+ STR.

Srinivas C, Bhaskar Rao D, Yesubabu V, Baskaran R and Venkatraman B 2013 Tropical cyclone predictions over the Bay of Bengal using the high-resolution advanced research weather research and forecasting (arw) model; *Quart. J. Roy. Meteorol. Soc.* **139(676)** 1810–1825.

Starzec M, Mullendore G L and Kucera P A 2018 Using radar reflectivity to evaluate the vertical structure of forecast convection; *J. Appl. Meteorol. Climatol.* **57(12)** 2835–2849.

Sun Y, Dong X, Cui W, Zhou Z, Fu Z, Zhou L, Deng Y and Cui C 2020 Vertical structures of typical meiyu precipitation events retrieved from GPM-DPR; *J. Geophys. Res. Atmos.* **125(1)** e2019JD031466.

Taraphdar S, Mukhopadhyay P, Leung L R, Zhang F, Abhilash S and Goswami B 2014 The role of moist processes in the intrinsic predictability of Indian ocean cyclones; *J. Geophys. Res. Atmos.* **119(13)** 8032–8048.

Taylor K E 2001 Summarizing multiple aspects of model performance in a single diagram; *J. Geophys. Res. Atmos.* **106(D7**) 7183–7192.

Tewari M, Chen F, Wang W, Dudhia J, LeMone M A, Mitchell K, Ek M, Gayno G, Wegiel J and Cuenca R H 2004 Implementation and verification of the unified NOAH land surface model in the WRF model; 20th conference on weather analysis and forecasting/16th conference on numerical weather prediction **1115(6)**.

Thompson G, Field P R, Rasmussen R M and Hall W D 2008 Explicit forecasts of winter precipitation using an improved bulk microphysics scheme. Part II: Implementation of a new snow parameterization; *Mon. Weather Rev.* **136(12)** 5095–5115.

Yamaguchi M, Ishida J, Sato H and Nakagawa M 2017 Wgne intercomparison of tropical cyclone forecasts by operational NWP models: A quarter century and beyond; *Bull. Am. Meteorol. Soc.* **98(11)** 2337–2349.

Yano J I, Geleyn J F, Köhler M, Mironov D, Quaas J, Soares P M, Phillips V T, Plant R S, Deluca A and Marquet P *et al.* 2015 Basic concepts for convection parameterization in weather forecast and climate models: COST Action ES0905 final report; *Atmosphere* **6(1)** 88–147.

Zhu T and Zhang D L 2006 Numerical simulation of hurricane bonnie (1998). Part II: Sensitivity to varying cloud microphysical processes; *J. Atmos. Sci.* **63(1)** 109–126.

Corresponding editor: Parthasarathi Mukhopadhyay